Cell Reports
Methods

Article

Immune response to adeno-associated viral vectors in a human iPSC-derived microglia chimeric mouse model

Graphical abstract

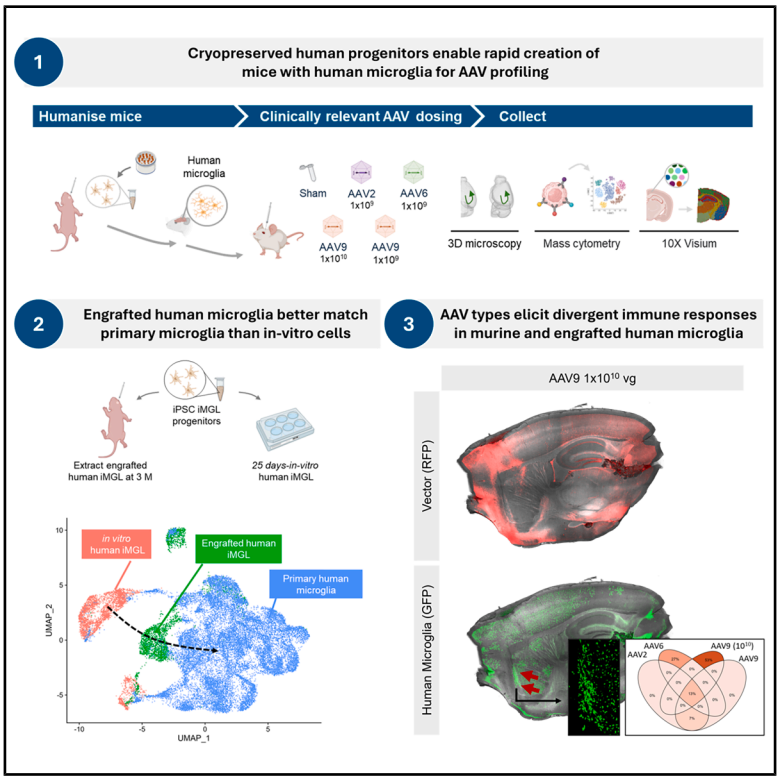

Highlights

- Cryopreserved human precursors generate mice with human microglia across the CNS
- Engrafted human microglia resemble primary microglia better than *in vitro* differentiated cells
- Human microglia in chimeric mice remain functional, responding to stimuli and phagocytosis
- AAV serotypes elicit divergent immune responses in mouse microglia and human microglia

Authors

Jan R. Detrez, Caroline Eykens, Gaëlle Gillet, ..., Julien Gasser, Luke M. Healy, Irena Kadiu

Correspondence

jan.detrez@ucb.com

In brief

Detrez et al. generate a human microglia chimeric mouse model in which human microglia, generated from cryopreserved precursors, engraft in the mouse CNS, adopt primary human microglial features, and maintain functional responsiveness. This chimeric model reveals that AAV serotypes elicit divergent immune responses in mouse microglia and human microglia.

Detrez et al., 2026, Cell Reports Methods 6, 101362
April 20, 2026
https://doi.org/10.1016/j.crmeth.2026.101362

CellPress

Cell Reports Methods

CellPress
OPEN ACCESS

Article

Immune response to adeno-associated viral vectors in a human iPSC-derived microglia chimeric mouse model

Jan R. Detrez,[1,4,*] Caroline Eykens,[1] Gaëlle Gillet,[1] Manisha Padmakumar,[1] Sílvia Cabré,[1] Phil Stanley,[2] Julien Gasser,[1] Luke M. Healy,[1] and Irena Kadiu[1,3]

[1]Neuroinflammation Focus Area, Neuroscience Research, UCB, Braine-l'Alleud, Belgium
[2]Early Development Statistics, UCB, Slough, UK
[3]Senior author
[4]Lead contact
*Correspondence: jan.detrez@ucb.com
https://doi.org/10.1016/j.crmeth.2026.101362

MOTIVATION Adeno-associated virus (AAV)-based gene therapy for severe neurological diseases is challenged by immune responses, which are difficult to study accurately in genetically divergent rodent models or in *in vitro* human iPSC-derived microglia (iMGL) that acquire activated phenotypes lacking complex brain environment cues. To address these translational gaps, we generated human microglia chimeric mice in which the iMGL are provided with complex CNS cues, ensuring that engrafted cells more closely resemble primary human microglia compared to their *in vitro* counterparts. Furthermore, to overcome the logistical and yield challenges of lengthy chimeric protocols, we developed a high-yield iMGL differentiation protocol featuring a cryopreservation stopping point at the iHPC stage.

SUMMARY

Adeno-associated virus (AAV)-based gene therapy for severe neurological diseases is challenged by immune responses, which are difficult to study accurately in genetically divergent rodent models or in *in vitro* human induced pluripotent stem cell (iPSC)-derived microglia (iMGL) that acquire activated phenotypes lacking complex brain environment cues. To address this, we generated human microglia chimeric mice. We developed a high-yield iMGL differentiation protocol incorporating a cryopreservation stopping point at the induced hematopoietic precursor cell (iHPC) stage, which increased flexibility and enabled a high level of chimerism. Engrafted iMGL transcriptionally and phenotypically resembled primary human microglia and were functionally active, displaying phagocytosis and immune response to inflammatory stimuli. Assessment of AAV serotypes revealed that murine microglia induced a larger immune response compared to human iMGL, cautioning against overinterpreting inflammatory responses in rodent models. This model provides a critical tool to define the human immune response to AAVs early in vector discovery.

INTRODUCTION

Interest in gene therapy has been re-kindled in recent years. Successes of adeno-associated virus (AAV) therapies in spinal muscular atrophy and congenital retinal dystrophies have laid the foundation for therapeutic applications in broader patient populations. While these outcomes have the potential to be applied to other mono- and polygenic neurological diseases, some obstacles stand in the way of meaningful therapeutic impact. Beyond technical hurdles associated with delivery, biodistribution, and cell tropism, the immune response to gene delivery vectors and foreign transgene products remains an important challenge to AAV-based gene therapy.[1] Two major immunological challenges have been recognized in the AAV gene therapy field. The first is the presence of pre-existing neutralizing antibodies resulting from prior natural AAV infections, which limits patient eligibility for clinical trials and therapeutic efficacy. The second major concern involves immune-related hepatotoxicity observed in high-dose systemic treatments, attributed to significant vector accumulation in the liver. In addition to these well-established challenges, AAV administration to the central nervous system (CNS) can also elicit innate immune activation, including a microglial pro-inflammatory response. While not yet considered a major limitation for clinical application, such glial reactivity could influence transgene expression and potentially exacerbate underlying

neuroinflammatory conditions. A deeper understanding of these CNS-specific immune interactions is therefore critical to ensure both the efficacy and safety of AAV-based therapies for neurological diseases. Studies have shown that high titers of AAV disrupt cerebrovascular integrity, increase peripheral infiltration, and induce glial activation in preclinical models of neurological disease.[2,3] Although, viral titer modeling from rodent to human can mitigate certain aspects of the inflammatory response from rodent glia, preclinical models may skew biological insights into immune-AAV interactions. A better understanding of the limitations of mouse models is critical, considering their continued extensive use in preclinical research in general and gene therapy programs in particular. Their utility beyond complex organ or system crosstalk needs to be carefully considered, given their limited display of the full range of disease pathobiology.[4] This stems from the low gene homology and divergent function of a substantial portion of immune regulatory genes in mouse and human inflammatory responses.[5]

Human induced pluripotent stem cell (iPSC)-derived microglial-like cells (iMGL) have become an indispensable tool in drug discovery, aiming to fill the translational gap between rodent models and human disease.[5] Although iMGL are primary human microglia-like in certain aspects, when cultured *in vitro*, these cells are deprived of critical environmental cues, including contextual crosstalk with other CNS-resident cells that define their phenotype and function.[6] To provide iMGL with more physiological complex cues and capture any synergies of microglial-neuron, microglial-astrocyte, and oligodendroglia crosstalk in response to AAV, we generated chimeric mice with brains and spinal cords colonized by human iMGL. Chimeric iMGL mouse models have been recently reported in the literature, laying the foundation for the generation of potentially more translatable models that capture human cell behavior in a more complex environment[6–10]. However, their reliance on lengthy and labor-intensive methods for the generation of human iMGL introduced a plethora of logistic challenges, hindering their use in a drug discovery setting. Therefore, we developed a high-yield human iMGL differentiation protocol, including a stopping point of cryopreservation at the induced hematopoietic precursor cell (iHPC) stage prior to implantation. This approach reduced the planning complexity of *in vivo* chimerization while minimizing variability in differentiation and culture contamination risk prior to chimerization campaigns. We demonstrate here that our approach results in successful colonization of human iPSC-derived microglia across brain regions without inducing overt perturbations at the molecular and cellular levels in the host brain. We demonstrate that iMGL colonize the murine spinal cord within 6 weeks post-transplantation, suggesting pan-CNS chimerism that could be relevant for modeling a broader range of neurological conditions. Furthermore, we show that engrafted iMGL, characterized *ex vivo* by single-cell resolution mass cytometry and transcriptomic analysis, express canonical primary human microglia markers, clustering closer to primary human cells compared to their *in vitro* cultured counterparts. These cells are functionally active *in vivo*, exhibiting cytokine responses to inflammatory stimuli and phagocytic uptake of bioparticles in acute adult chimeric organotypic brain cultures. Lastly, we characterize, through light-sheet microscopy and spatial transcriptomics, human and murine microglia and astroglial responses to various AAV serotypes used for gene therapy. Our data indicate that human microglia display a more attenuated immune response at clinically relevant AAV doses compared to their murine counterparts, cautioning against overinterpretation of inflammatory and immune responses in rodent models of disease used for gene therapy studies.

RESULTS

iMGL from cryopreserved iHPC are phenotypically distinct from human blood monocytes and express primary microglia markers

Generation of CNS chimeric mice requires large numbers of iMGL and flexibility in the timing of iPSC cultures and NOD scid gamma (NSG) mouse litters. Current protocols have limited cell yields and require long-term culturing of cells.[6,7,9] Therefore, our first goal was to establish a differentiation protocol amenable to scale-up to overcome the yield bottleneck, with a cessation point for cryopreservation at the iHPC stages for increased flexibility (S1A). iPSCs harboring a GFP reporter under the Iba1 promoter were grown in AggreWell 400 plates (with 5900 microwells per well), amounting to ~354.000 embryoid bodies and yielding more than 5×10^8 iPSC-derived hematopoietic stem cells from a differentiation campaign at day 10, representing a 40-fold increase in yield (S1B). iHPCs generated from several harvest rounds were cryopreserved for subsequent engraftment studies.

To determine whether the iMGL generated from our modified protocol were microglial-like, we performed phenotypic characterization at single-cell resolution by mass cytometry at day 24, when these cells start to acquire a microglia-like ramified morphology (S1B). The monocyte population present in human peripheral blood mononuclear cells (PBMCs) was used as a comparator for the myeloid lineage. Data show that iMGL at day 24 of differentiation cluster separately from primary human monocytes and express canonical human pan-leucocytic and microglia markers CD45, CD11b, CX3C motif chemokine receptor 1 (CX3CR1), EGF-like module-containing mucin-like hormone receptor-like 1 (EMR1), as well as regulators of antigen presentation and immune response (HLA-A, HLA-B, HLA-C, HLA-DR, CD86, CD11c), phagocytosis (CD64, CD36, CD16), and neuronal crosstalk (CD95) (S1C).

iMGL from cryopreserved iHPC display phagocytic and migratory capacity *in vitro*

Next, we questioned whether iMGL display essential microglia-like functions such as phagocytosis, directed migration, and response to various inflammatory stimuli. The iPSC parental line (ASE-9109), from which the GFP reporter line used for engraftment studies was derived (ASE-9109-GFP), was included in functional assays to ascertain the impact of GFP expression under the Iba1 promoter on critical iMGL functions. To determine whether iMGL are phagocytic, cells were exposed to zymosan pH-responsive rhodamine bioparticles that fluoresce red upon internalization into acidified endolysosomal compartments. Phagocytic uptake was monitored by time-lapse imaging in the presence or absence of cytochalasin D (an actin cytoskeleton disruptor) over 24 h. Both the parental and reporter lines

CellPress
OPEN ACCESS

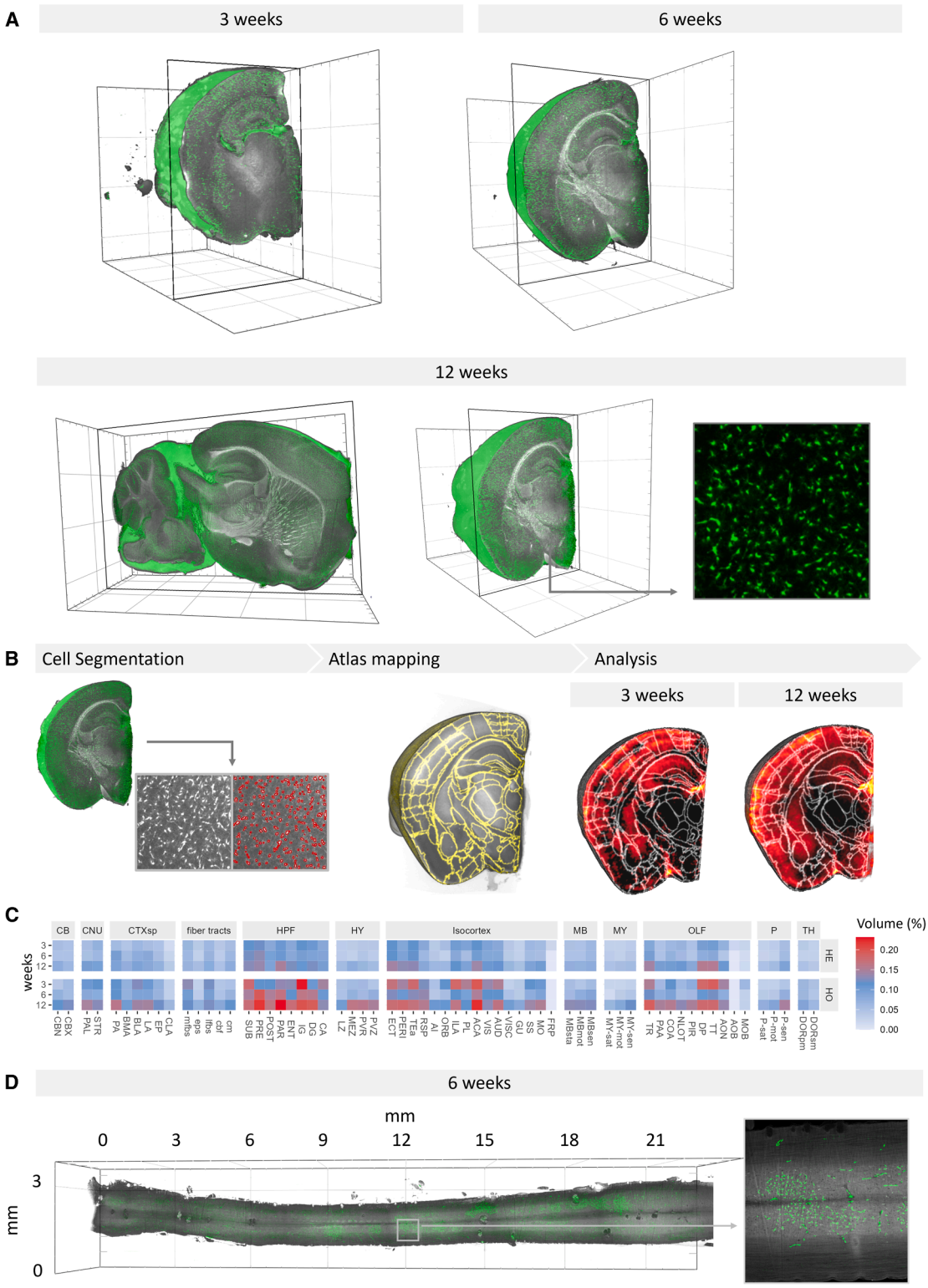

(legend on next page)

displayed robust phagocytic activity, and genetic modification does not interfere with this function (Figure S1D; Video S1).

Cell migration toward a chemoattractant such as adenosine diphosphate (ADP), typically released under neuronal metabolic stress or injury, was tested by monitoring directed movement of iMGL through a porous membrane separating the top and bottom wells of a chemotaxis chamber.[11] Incremental concentrations of PSB0739, a purinergic receptor P2Y12 antagonist, were used to pharmacologically validate chemotactic activity. Migratory activity was confirmed by the disappearance of iMGL from the top surface of the plasma membrane for both parental and GFP reporter lines. These data, together with a dose-dependent response to PSB0739 blockade of chemotactic activity, demonstrate that iMGL can migrate toward a chemotactic stimulus (Figure S1E).

iMGL from cryopreserved iHPC are responsive to inflammatory stimuli *in vitro*

Next, we questioned whether iMGL can respond to inflammatory stimuli *in vitro*. Cells challenged with liposaccharide (LPS) were analyzed by mass cytometry to assess the immune response. Eight clusters with varying levels of expression of innate and microglial cell surface markers were identified, suggesting distinct states of maturity of iMGL at day 24 of differentiation in culture (Figure S2A). Exposure to incremental doses of LPS resulted in diminishing cell numbers in clusters 5 (immature and low in microglial markers) and 7 (intermediate expression of activation and myeloid markers; Figures S2B and S2C). Cluster 2, expressing high levels of CX3CR1 and other regulators of phagocytic, antigen presentation, and Toll-like receptor (TLR)-mediated functions, increased with LPS stimulation (Figures S2B, S2C). Overall microglial population analysis revealed decreased levels of mean signal intensity (MSI) for Triggering Receptor Expressed on Myeloid Cells 2 (TREM2) and increased levels of scavenger receptors, antigen presentation markers, and TLRs in the engrafted iMGL, suggesting they can respond to inflammatory stimuli *in vitro* (Figure S2D).

iMGL differentiation protocol increases experimental flexibility without compromising engraftment efficacy

In recent years, several studies have reported successful brain engraftment of iMGL in various transgenic immunodeficient mouse models. While chimerism in these studies was achieved,[6,7,9] the proposed protocols, based on non-stop differentiation from iPSC to iMGL for 25 days followed by immediate implantation in postnatal stage day 2–3 litters, represent several challenges. First, iPSC lines from healthy or diseased donors tend to differentiate at different rates and are often prone to contamination due to lengthy culturing conditions. Second, the non-cessation protocols do not allow for phenotypic and functional quality control assessment of cells at various stages of differentiation and prior to engraftment. Third, timing of the lengthy protocols with the birth of litters and considering the dynamic nature of drug discovery would exclude use of this model as is for drug testing studies. To address these challenges, we established a high-yield protocol involving cryopreservation of cells at the iHPC stage and their differentiation to immature iMGL (as needed) for 2–3 days prior to engraftment campaigns. NOD.Cg-*Prkdc*^{scid}*IL2rg*^{tm1Wjl}/SzJ human colony-stimulating factor 1 (NSG-hCSF1) were chosen for the engraftment studies. These mice express hCSF1, which sustains survival and proliferation of engrafted iMGL. Furthermore, these mice lack adaptive peripheral immune cells, including T cells, B cells, and natural killer (NK) cells implicated in host-versus graft responses (Figure S3).

To ascertain whether iMGL generated from cryopreserved iHPCs were efficiently engrafted in the NSG-hCSF1 mice, we compared our protocol with the non-cessation MIGRATE method reported by Fattorelli et al.[7] We replicated the MIGRATE differentiation protocol, as demonstrated by the quality of embryoid bodies and iHPC culture (Figure S4A). Mass cytometry analysis performed on chimeric mouse brains to define the numbers and phenotypes of mouse and human microglia populations showed ~20% chimerism and similar iMGL cell surface phenotypes at 6 weeks post-engraftment for both UCB and MIGRATE protocols (Figure S4B). Our data demonstrate that cryopreservation cessation at the iHPC stage results in similar chimerism and cellular phenotypes of extracted iMGL as the non-cessation protocol, enabling future studies with a lower logistical burden.

iMGL achieve high chimerism in brain and spinal cord

Next, we investigated an optimal dosing window to enable assessment of the human microglial response to various AAV serotypes used for gene therapy delivery. Broad regional chimerism was a pre-requisite in this study to enable suitable iMGL and AAV spatial overlap and, consequently, more accurate measurement of microglial responses to the various serotypes. We assessed iMGL colonization at 3-, 6-, and 12-week post-engraftment by light-sheet microscopy imaging of the brain and spinal cord. Images demonstrate iMGL (GFP/green) presence in several brain regions at 3 weeks post-engraftment, increasing in numbers and showing broader regional coverage at 6- and 12-weeks post-engraftment (Figure 1A; Video S2). Brain segmentation and volumetric analysis show that iMGL can migrate to various brain regions, where they acquire a ramified morphology (Figures 1A and 1B). The highest chimerism was observed in the hippocampal formation, isocortex, and olfactory regions of the homozygous (HO) mice (Figures 1B and 1C). Interestingly, human cell colonization expanded beyond the brain, with iMGL migrating into the spinal cord. While this was

Figure 1. Light-sheet microscopy of chimeric mice reveals time-dependent iMGL brain colonization

(A) Representative 3D renderings from the longitudinal study show increased integration of iMGL across brain regions over time.

(B) An automated image analysis script was setup for cell segmentation and brain atlas mapping, allowing regional mapping through 3D heatmaps, and quantification of iMGL integration.

(C) Quantification of iMGL volume per brain region demonstrates increased integration over time, with higher integration efficiency achieved in CSF1^{HO} animals.

(D) Representative 3D rendering shows iMGL integration in the mouse spinal cord. $N = 9/1$ for CSF1^{HE}/CSF1^{HO} and $N = 9/3$ and $N = 8/5$ mice at 3, 6, and 12 weeks, respectively. Allen Brian Atlas abbreviations are listed in Table S1.

CellPress
OPEN ACCESS

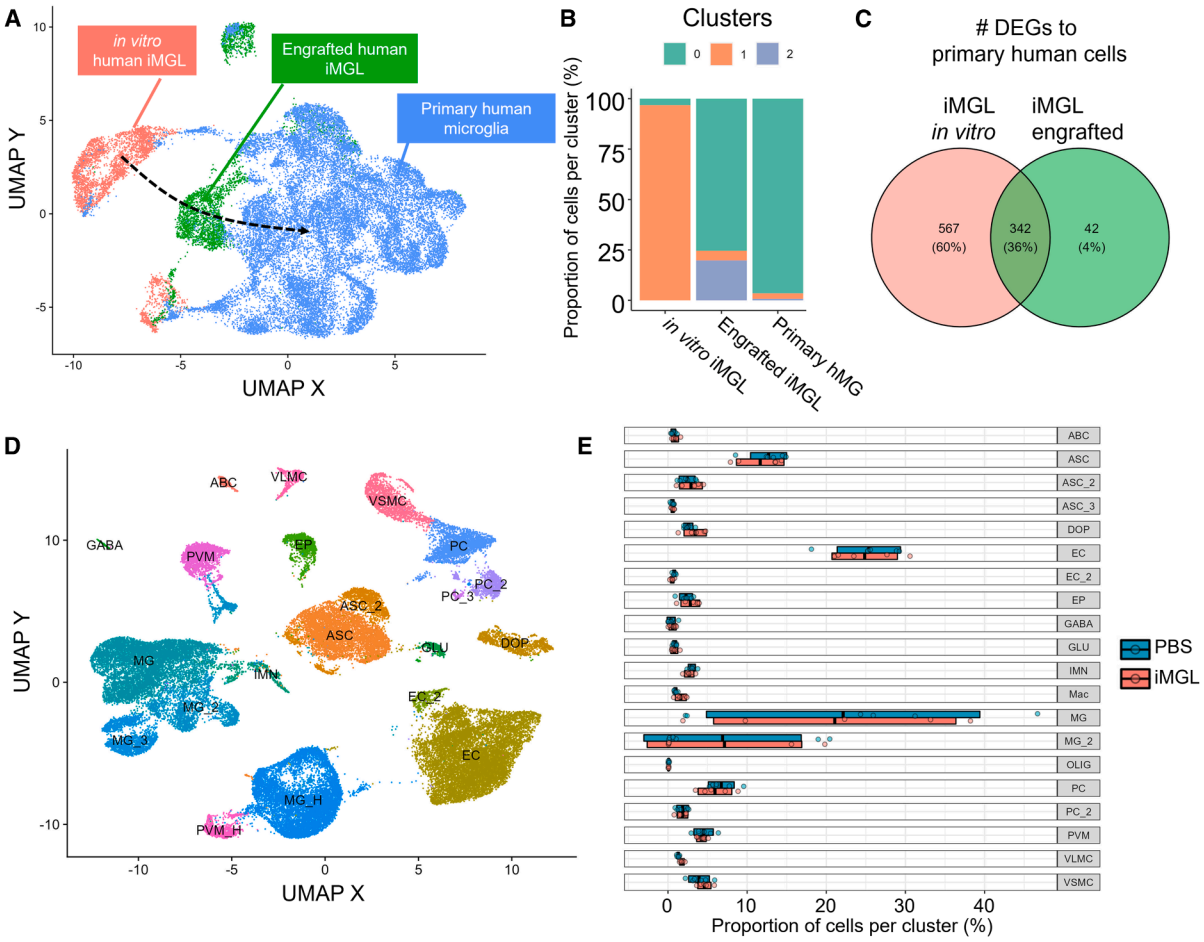

(legend on next page)

observed earlier,[6] reconstructed 3D light-sheet images reveal that iMGL colonize the entire length of the spinal cord, with higher levels of chimerism observed in the sacral segments (Figures 1D; S4; Video S3). We demonstrate that human iMGL can colonize various brain regions and the spinal cord within 12 weeks of engraftment, enabling broad exposure to the AAVs. Furthermore, this opens new possibilities for the generation of diseased iMGL chimeric models with spinal cord pathology involvement.

Engrafted iMGL differ transcriptionally from *in vitro* cultured iMGL, and their presence triggers limited responses in host brain resident cells

A key aim of this study is to understand how human microglia might react to AAV gene therapy vectors in a clinical setting. Therefore, we questioned whether complex host brain cues acting on engrafted iMGL induce primary human microglial characteristics. We performed single-cell transcriptomic analysis comparing iMGL cultured *in vitro*, engrafted iMGL, and primary human microglia.[8] Chimeric mouse brains were processed using a dissociation method that allows for retention of brain resident cells beyond microglia.[12] In addition, we confirmed inhibition of an *ex vivo* activation signature with this protocol and continued the use of this method for all single-cell studies (Figure S5).[12] Single-cell transcriptomics analysis of iMGL grown *in vitro* at 25 days *in vitro* (DIV) and engrafted iMGL at 12 weeks post-engraftment revealed distinct clustering of *in vitro* iMGL, engrafted iMGL, and primary human microglia. Analysis of overall population representations indicated a common cluster 0, represented >90% of the overall population in primary human microglia and ~5% and 75% in iMGL *in vitro* and engrafted, respectively (Figures 2A and 2B). We first identified differentially expressed genes (DEGs) by comparing primary human cells to both *in vitro* and engrafted iMGL, then used a Venn diagram to assess the overlap. This analysis showed that 36% of the total DEGs were common to both comparisons, while the *in vitro* group had a 60% unique divergence and the engrafted group had a 4% unique divergence (Figure 2C). These data highlight differential cell states of iMGL cultured *in vitro* compared to chimeric and primary human microglia, which cluster closer together, further emphasizing the importance of complex CNS cues on microglial identity.

Next, we investigated whether implantation of iMGL introduces any perturbations in mouse brain homeostasis. Assessing murine brain resident cell responses to the human graft is informative for understanding the model in general but more importantly for establishing a baseline to benchmark against any AAV-induced responses. Mouse brain resident cell transcripts were extracted, re-clustered, and cell population representation was captured as the proportion of cells relative to the entire brain resident population. Data show that iMGL did not induce changes in cell counts across populations of brain resident cells (Figures 2D and 2E). A limited number of DEGs were metabolic and endo-lysosomal transport DEGs in the neuroepithelial lining of the ventricles (ependymal cells) and blood-brain barrier (BBB) vascular endothelium, suggesting potential implications for BBB integrity. Interestingly, genes such as CD209a and C4B, regulating immune tolerance and inflammatory responses to tissue injury by tissue macrophages or microglia and astrocytes, respectively, were increased, suggesting potential tissue remodeling activity in transplanted brains. Limited changes in transcriptomic profiles of other brain resident cells, including neurons and oligodendrocytes, suggest that implanted iMGL do not significantly perturb the host's brain environment (Figure 2F).

High-dimensional mass cytometry characterization at single-cell resolution shows engrafted iMGL increase in numbers and heterogeneity over time in naive chimeric mice

Next, we performed mass cytometry analysis of chimeric mouse brain homogenates to assess activation states of human and murine microglia at the protein level and at single-cell resolution in aging chimeric mice. FlowSOM clustering identified distinct murine (clusters 1 and 5) and human (clusters 2–4) microglial populations (Figures S6A; 3A). A significant increase in overall numbers of iMGL was observed at 6- and 12-weeks post-engraftment compared to the 3-week time point in HO mice (Figure S6B). Engrafted iMGL represented 80% of the overall myeloid ($CD45^+$) population at 12 weeks in the $CSF1^{HO}$ mice (Figures 3B and 3C; S6B). At 3 and 6 weeks, iMGL were predominantly found in cluster 2 (pan CD45 and CD11b/c). At 12 weeks, significant increases in cell numbers were observed in iMGL clusters 3 and 4. Phenotypic characterization of these clusters revealed significantly higher expression levels of several human

Figure 2. Engrafted iMGL more closely resemble primary human microglia than *in vitro* iMGL and induce changes in the transcriptomics profile of host brain cells

(A) Uniform manifold approximation and projection (UMAP) representation of single-cell data indicates greater resemblance of chimeric mice iMGL to primary human microglia, relative to *in vitro* cultured iMGL. (n = 1 *in vitro* iMGL at 25 DIV, n = 4 iMGL from 2-month-old chimeric mice, n = 7 primary human microglia from GSE108476).

(B) Low-resolution clustering reveals that chimeric mice iMGL and primary human microglia share a common cluster, which is not present in *in vitro* cultured iMGL.

(C) DEG analysis at the cellular level using Seurat FindMarkers shows that *in vitro* cultured iMGL exhibit a higher number of DEGs (342 + 567 DEGs) compared to engrafted iMGL (342 + 42 DEGs), with cut-offs set at corrected p value at 0.05 and absolute log10-fold change at 1.

(D) UMAP plot of the experiment comparing chimeric mice and sham-injected mice, with distinct brain cell types annotated. (N = 5 iMGL-injected (chimeric mice), N = 6 sham-injected $CSF1^{HO}$ controls at 3 months of age).

(E) Assessment of the proportion of cells in each cluster, after removing the human cluster and re-clustering the data, indicates no notable shifts in cluster sizes (means ± SEM). Dots represent individual mouse data points.

(F) Pseudo-bulk DEG analysis shows the up- and downregulation of genes in chimeric mice compared to sham-injected control mice for distinct cell types.

Abbreviations are as follows: ABC, arachnoid barrier cells; ASC, astrocytes; DOP, dopaminergic neurons; EC, endothelial cells; EP, ependymal cells; GABA, GABAergic neurons; GLU, glutamatergic neurons; iMN, immature neurons; Mac, macrophages; MG, microglia; OLIG, oligodendrocytes; PC, pericytes; PVM, perivascular macrophages; VLMC, vascular leptomeningeal cell; VSMC, vascular smoot muscle cells.

CellPress
OPEN ACCESS

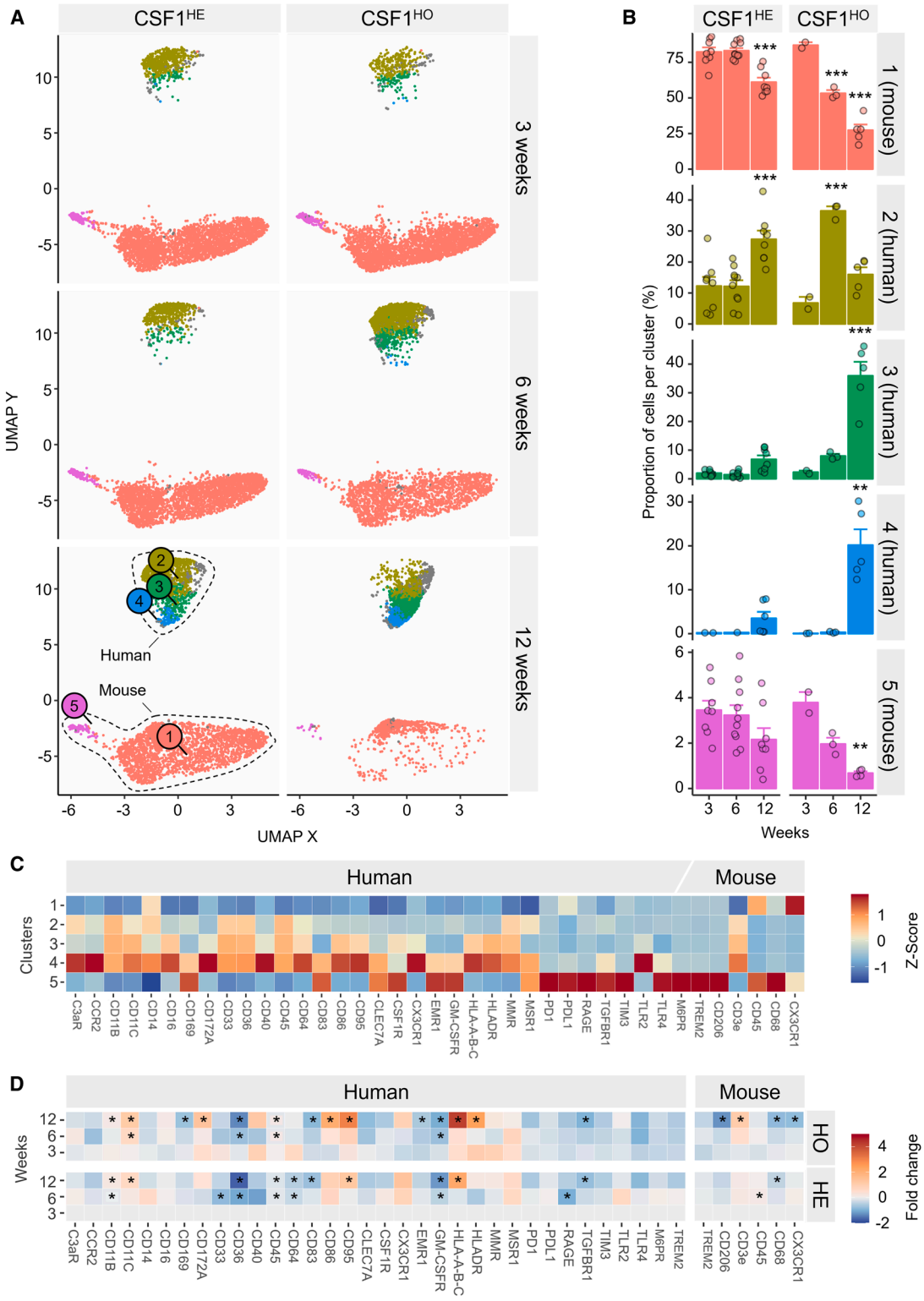

Figure 3. Complex brain environmental cues induce a phenotypic shift in colonizing iMGL

(A) UMAP plots of brain data per genotype and time point shows that the proportion of cells per clusters shifts over time and across genotypes.

(B) The proportion of cells per cluster was extracted and shown as bar plots with means ± SEM, with dots representing individual animals. The *p* value is based on an ANOVA test per cluster compared to the control ($CSF1^{HE}$ at 3 weeks) using Dunnett's test post-hoc test.

(legend continued on next page)

microglial and pan-leucocytic canonical markers,[13] antigen presentation (HLA-A, HLA-B, HLA-C, HLA-DR, CD86), phagocytosis markers (CD64, CD36, CD16), and neuronal crosstalk marker CD95, among others (Figures 3D; S6C).

Engrafted iMGL mount an inflammatory response to systemic inflammatory stimuli and actively phagocytose bioparticles *ex vivo*

Having characterized the baseline expression levels of human microglia canonical markers in naive chimeric mice *in vivo*, we next questioned whether these cells maintain functional activity *in vivo*. Determining whether the model is responsive to exogenous stimuli is particularly important to enable the exclusion of any false-negative outcomes in the context of AAV exposure. LPS was selected as a trigger for CNS inflammation based on its propensity to trigger murine and human microglial inflammatory responses when injected systemically in both mice and humans.[14,15] Chimeric mice at 12 weeks post-engraftment were injected intraperitoneally (i.p.) with LPS, and 24 h post-injection, immune cell subsets (human and mouse) present in the brain homogenate were characterized by mass cytometry. Unsupervised clustering confirmed the presence of distinct human (clusters 1–3) and murine (clusters 4–6) microglial populations (Figure 4A). LPS exposure induced a phenotypic shift, resulting in a significant decrease in cluster 1, classified as immature iMGL expressing higher levels of CD11b, CD11c, CD33, and CD45. Significant increases in iMGL numbers expressing high levels of activation markers, including scavenger receptors CD16, CD36, CD64, CD95, antigen presentation regulators such as CD40, CD83, CD86, HLA-A,B,C, CX3CR1, and HLA-DR, were observed in human clusters 2 and 3 in chimeric mice exposed to LPS (Figures 4B–4D). Interestingly, cluster 5, representing most of the murine microglial population, was reduced with LPS treatment. Cluster 4, likely comprising the other myeloid cells of the brain such as perivascular, choroid plexus, and meningeal macrophages or dendritic cells ($C3AR^+$, $CCR2^+$, $CSF1R^+$, $GM\text{-}CSFR^+$), was significantly decreased, while cluster 6, characterized by lower pan-leukocytic and activation markers, increased significantly (Figures 4B–4D). These data suggest that human microglia are responsive to inflammatory stimuli and diverge in their response compared to murine myeloid brain resident cells.

Next, we assessed the phagocytic activity of iMGL in acute brain organotypic cultures from chimeric mice at 12 weeks post-engraftment. Chimeric mouse brain sections were exposed to pH-responsive rhodamine-conjugated zymosan particles to further validate phagocytic activity.[16] Bioparticle uptake in both cell types was assessed using several parameters, including the number of cells positive for pH-responsive rhodamine signal, the ratio of phagocytic microglia to the overall cell number, and the number of bioparticles/cell (Figure 4E). Data show that both human and mouse microglia actively uptake zymosan particles. A higher absolute number of phagocytic murine microglia was observed in the organotypic brain sections; however, when compared to their respective overall populations, phagocytic iMGL were significantly more represented. Furthermore, iMGL showed a significantly higher uptake capacity (bioparticles/cell) compared to murine cells (Figure 4E). These data overall demonstrate that engrafted iMGL are functionally active, suggesting that the chimeric model is likely to be responsive to additional exogenous stimuli such as AAV.

Light-sheet microscopy confirms regional overlap in iMGL engraftment and AAV biodistribution

Having confirmed that iMGL engraft successfully in the brain and can elicit immune and other functional activities upon stimulation, we next assessed regional overlap between iMGL and AAV. Spatial proximity of AAV to iMGL was a pre-requisite for assessing immune responses to various serotypes. Chimeric mice at 16 weeks post-engraftment were injected intrastriatally with AAV2 (1×10^9 viral genomes [vg]), AAV6 (1×10^9 vg), and AAV9 (1×10^9 and 1×10^{10} vg). The dose of 1×10^9 vg was modeled for mice based on dosing regimen used in humans.[17] An additional dose of AAV9 at 1×10^{10} vg was selected to assess immune response at titers previously reported to induce inflammatory responses.[2]

Light-sheet microscopy 3D reconstruction of chimeric brains stained with anti-red fluorescent protein (RFP) antibodies demonstrates broad reginal distribution for each serotype (Figure 5A; Video S4). Staining with the cross-species IBA1 antibody visually confirmed microglial activation. This was apparent in the AAV9 1×10^{10} condition (Figure 5C), and an overall increase in IBA1 signal intensity could also be observed in the regional quantification of these data (Figure 5D). Using an anti-GFP antibody targeting human cells, we were able to isolate human microglia and reveal that this microglial response was mostly driven by mouse microglia, with only a minor visual contribution from human iMGL (Figure 5C). This IBA1 signal colocalized with the RFP reporter signal at the injection site, which displayed elevated levels of RFP, but such colocalization was also observed in remote areas (Figures 5C and 5D).

AAV serotypes elicit divergent immune responses in murine and engrafted human microglia

Having characterized our iMGL and chimeric mice, we proceeded to use chimeric mice to assess the safety profile of different AAV serotypes (AAV2, AAV6, and AAV9) on the host brain and the engrafted iMGL. Mice were engrafted at neonatal age, with the intrastriatal AAV transduction and tissue collections performed at 4 and 6 months of age, respectively.

Cytometry by time-of-flight (CyTOF) revealed no major changes in cell proportions within the mouse and human $CD45^+$ populations, indicating the absence of overt phenotypic switches (Figure S7A). Despite this, an overall increase in

(C) The normalized marker intensity per cluster is visualized in a heatmap.
(D) The fold change is compared to the control group ($CSF1^{HE}$ at 3 weeks) is shown in a tile plot, with asterisks indicating where the p value is below 0.05 based on an ANOVA with Dunnett's test post-hoc test. (N = 9/1 ($CSF1^{HE}$/$CSF1^{HO}$), N = 9/3, and N = 8/5 mice at 3, 6, and 12 weeks, respectively, with 10^5 events/sample targeted and 4,000 cells per group shown; $^*p < 0.05$; $^{**}p < 0.01$; and $^{***}p < 0.001$).

CellPress
OPEN ACCESS

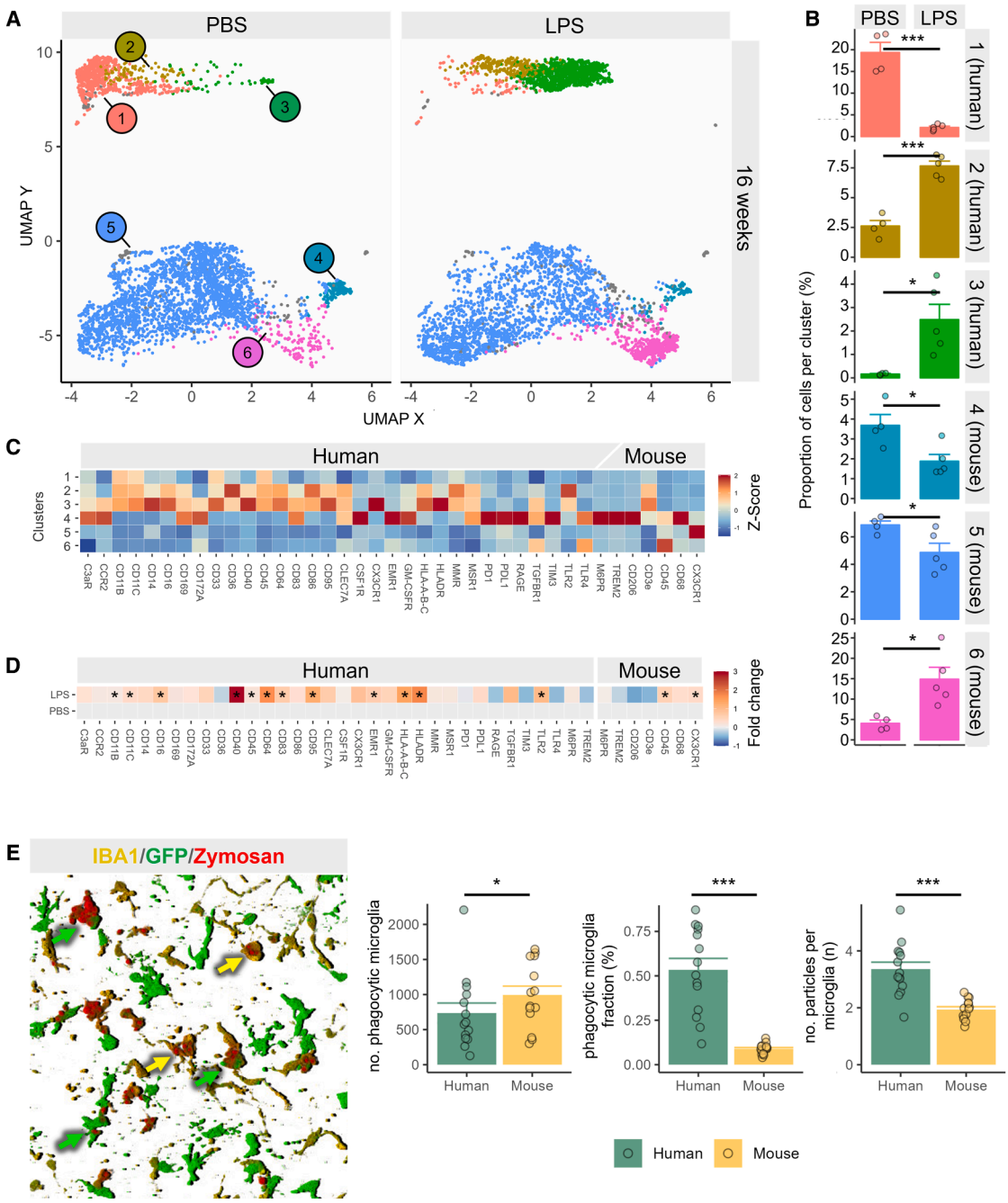

Figure 4. Engrafted iMGL respond to LPS and phagocytose Zymosan beads

(A) UMAP plots of brain data per treatment group are shown ($N = 4$ PBS and $N = 5$ LPS, using CSF1^{HO} animals aged 16 weeks, with 10^5 events/sample targeted and 4,000 cells per group shown).

(B) The proportion of cells per cluster was extracted and shown as bar plots with means ± SEM, with dots representing individual animals. The p values indicate significance based on ANOVA testing per cluster comparing LPS to PBS controls.

(C) The normalized marker intensity per cluster is visualized on a tile plot.

(D) The fold change compared to the control group (PBS) is shown on a tile plot, with asterisks indicating where $p < 0.05$ based on an ANOVA test per marker.

(E) Representative image of Zymosan bead uptake by human (green arrows) and mouse microglia (yellow arrows), with results from automated quantification of different experimental conditions. Points represent individual slices and bar plots are with means ± SEM, and statistical analysis was done using mixed model analysis ($N = 4$ CSF1^{HO} animals at 3 months, with 8 brain sections per pup). $p < 0.05$; $^{**}p < 0.01$; and $^{***}p < 0.001$.

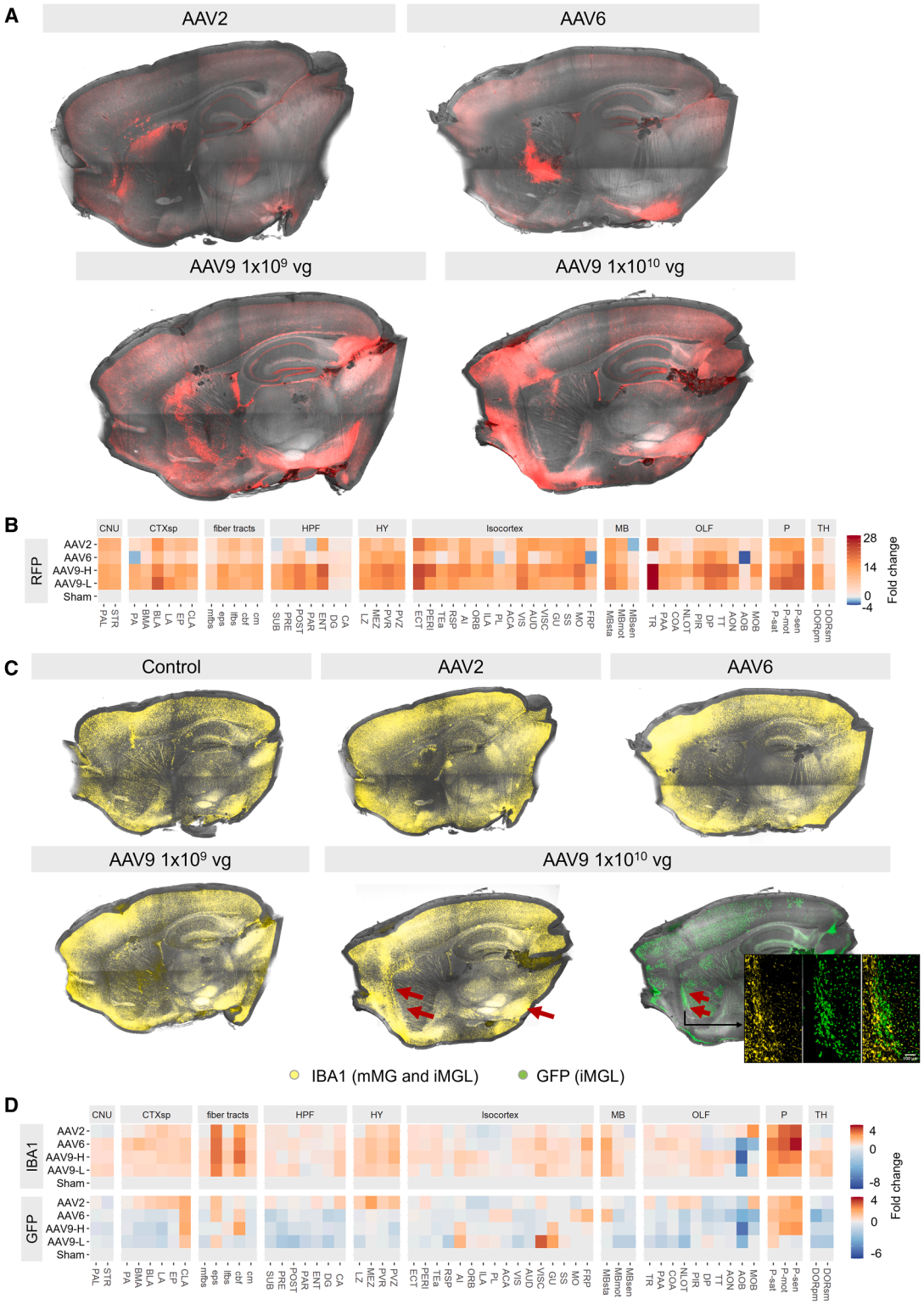

Figure 5. Visualization and quantification of light-sheet images reveals that mouse and human microglia respond to AAV injections

(A) 3D rendering of RFP signal across experimental conditions. RFP signal was processed by local background subtraction, and overlaid on the autofluorescence background channel. The same processing, brightness, and contrast settings were applied across all images. The RFP signal, expressed in transduced cells, is visible at the injection site and in interconnected brain regions.

(legend continued on next page)

intensity of markers targeting mouse and human microglia was observed across treatment conditions (Figure S7B). This increase was significant for AAV9 (human CD86) and AAV9 1×10^{10} vg (human CD86, human CX3CR1, and mouse CD68), indicative of microglial activation (Figure S7B).

Spatial transcriptomics analysis reveals serotype- and dose-dependent differential gene signatures in engrafted iMGL and mouse resident brain cells

Next, we performed spatial transcriptomics on brain sections of chimeric mice injected with the various AAV serotypes and doses to understand the regional responses of human and resident mouse microglia to AAVs. Spatial transcriptomics were performed near the injection site, as well as at a remote, caudal anatomical region (Figure 6A). A representative sample shows that more than 30,000 unique transcripts per spot were detected in dense cellular areas, indicative of a rich composition of the transcript library (Figure 6B). Image registration of the Allen Brain Atlas to the sample was performed to allow brain region-specific downstream analysis (Figure 6B). To explore the downstream effects of AAV administration, the spatial expression levels for established brain cell type markers were compared with the regional distribution of RFP transcripts. In the AAV9 1×10^{10} vg condition, a strong spatial colocalization of RFP expression with human microglia, mouse microglia, astrocytes, and to a lesser extent, oligodendrocytes was observed (Figure 6C). Regional quantification revealed a serotype-dependent increase in the number of spots detecting established genes representing human microglia (AAV6, AAV9 1×10^{9} vg, AAV9 1×10^{10} vg), mouse microglia (AAV2, AAV6, AAV9 1×10^{9} vg, AAV9 1×10^{10} vg) and astrocytes (AAV6, AAV9 1×10^{9} vg, AAV9 1×10^{10} vg) (Figure 6D). As the previous exploratory method relied on searching for pre-defined genes and discretization of the dataset into expressing and non-expressing spots, we next conducted a more unbiased analysis by calculating the Pearson correlation of RFP expression with all genes in our dataset (Figure 6E). The top 20 genes were extracted and annotated, showing that the majority originated from mouse microglial origin (69%), followed by astrocytes (12%) and oligodendrocytes (19%) (Figure 6F).

Next, we performed cluster analysis of the entire dataset, in which a shared AAV response cluster stood out among the treatment conditions (Figure 7A). This activation cluster was proportionally large in AAV9 1×10^{10} vg but also notable in AAV2, AAV6, and AAV9 1×10^{10} vg. Gene Ontology (GO) analysis of differentially expressed mouse microglia genes in this cluster revealed enrichment of pathways governing various immune system mechanisms (Figure 7B). They include the complement pathway, which aids in the destruction of pathogens; cytokine signaling pathways such as IL-6, JAK (Janus Kinase), STAT3, IL-2, and STAT5, which regulate immune cell activity; as well as interferon gamma and alpha responses, which play crucial roles in antiviral defense. Additionally, more general inflammatory response pathways are involved, coordinating immune responses to combat infections and maintain tissue homeostasis. Notably, even in mice with compromised immune systems, the allograft rejection pathway, responsible for rejecting foreign tissue, was heightened. In the investigation of human iMGL, we found that some pathways shared similarities with those observed in mouse models. However, due to the presence of only a small number of genes within each pathway, statistical significance was lacking. Notably, immune system pathways such as the complement pathway, interferon alpha and gamma pathways, and the previously mentioned signaling pathways were identified in both human iMGL and mouse profiles. We also found the allograft rejection pathway to be heightened in the engrafted human iMGL. Analysis of the top 20 markers that differentiate this cluster from the rest of the dataset showed that this cluster is largely dominated by human microglial genes (Figure 7C). This is in line with the Pearson correlation analysis performed earlier, which showed proportionally high levels of canonical human microglia markers. In addition to human microglia, the top genes of this AAV response cluster were derived from mouse microglia and astrocytes (Figure 7D).

To determine whether the genes compromising this response cluster are shared across treatment groups, DEG analysis was performed for each treatment, with sham-injected treatment samples serving as the reference group. The overlap between genes per treatment was summarized in a Venn diagram (Figure 7E). Considering that AAV9 1×10^{10} vg has the highest number of spots detected in the AAV response cluster, the largest amount of DEGs was observed in this group, followed by the AAV6 and AAV9 1×10^{9} vg group. The DEGs detected in the AAV9 1×10^{9} vg and AAV2 group were also detected in the AAV9 1×10^{10} vg condition. In contrast, for AAV6, 17% of genes did not overlap with those in the AAV9 1×10^{10} vg group.

Finally, samples distal from the engraftment site were evaluated. Following cluster analysis, an AAV response cluster could also be detected (Figure 7F). Similar to our primary analysis site, we also observed an activation cluster overlapping with the RFP injection site. In line with our findings from light-sheet microscopy, this indicates that AAVs can elicit an inflammatory response distal from their injection site.

DISCUSSION

This study sheds light on how human microglia respond to AAV vectors, which is important for understanding their potential in treating neurological diseases and how vector design affects inflammation in these conditions.[18] Brain-resident microglia

(B) Quantification of light-sheet fluorescence microscopy (LSFM) data for different injected AAV serotypes shows the mean distribution of RFP signal in tile plots, normalized to the control group ($N = 5$ per treatment group at 4 months of age) (C) Representative 3D renderings across AAV serotype treatments groups of IBA1 show visual concentration of microglia in the AAV injection and remote sites (red arrows) for AAV9 1×10^{10} vg. A modest increase in GFP signal, targeting human microglia, can be observed near the AAV injection site for AAV9 1×10^{10} vg (red arrows). Iba1 and GPF signals were processed by local background subtraction and overlaid on the autofluorescence background channel. The same processing, brightness, and contrast settings were applied across all images.
(D) Quantification of LSFM data for different injected AAV serotypes show the mean distribution of IBA1 and GFP signal in the tile plots, normalized to the control group ($N = 5$ per treatment group at 4 months of age). Allen Brian Atlas abbreviations are listed in Table S1.

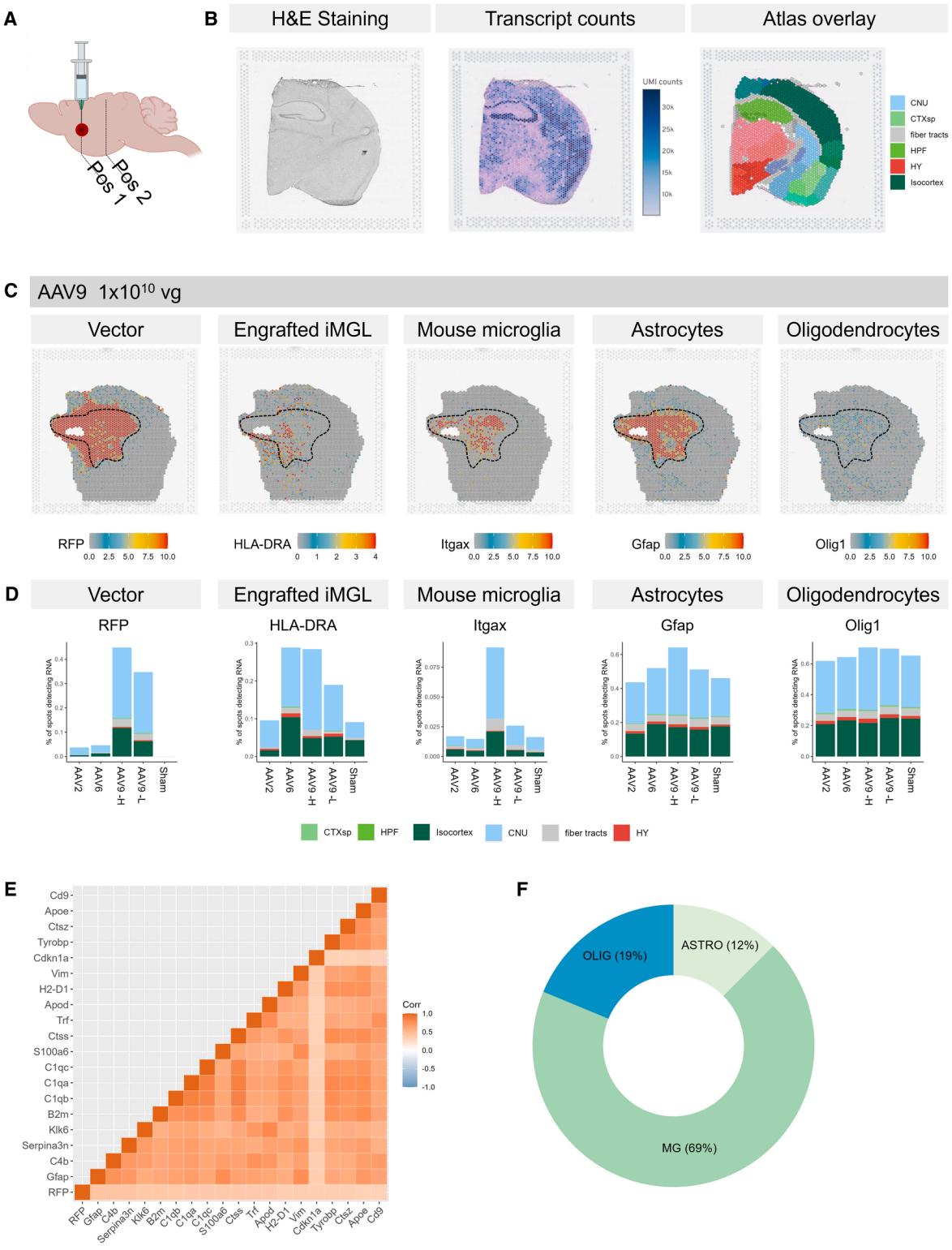

Figure 6. AAV serotypes elicit specific molecular signatures in human microglia and mouse brain resident cells

(A) Graphical representation of slice sampling for the spatial transcriptomics experiment. One slice per animal was sampled at the engraftment site (Sham chimeric $N = 3$, AAV2 $N = 3$, AAV6 with $N = 4$, AAV9 1×10^9 vg $N = 4$, AAV9 1×10^{10} vg $N = 3$) and at the remote distal site (control, $N = 1$, AAV9 1×10^9 vg $N = 1$, AAV9 1×10^{10} vg $N = 1$).

(legend continued on next page)

play a key role in mediating the host response to AAVs;[19] however, the study of microglia is particularly challenging due to i) the limited translational value of mouse models[8] and ii) the limited ability of cultured (iPSC-derived) human microglia to recapitulate *in vivo* microglial signatures and functions.[6] While microglia integrated into brain organoid models are considered more translationally relevant, they have been shown to also attain an unfavorable *in vitro* stress phenotype.[20] To address these challenges, we present a chimeric mouse model using transplanted human microglia and use this model to assess the innate brain immune response to four AAV serotypes at different dosages.

We have set up a high-yield iMGL generation protocol that allows for freezing of iHPC cells, reducing cell culture time before engraftment to just 3 days instead of weeks. Bulk freezing of cells reduces variability between differentiation rounds and decreases protocol failures that may results from the increased risk of cell culture contamination. Cryopreservation has been utilized for archiving primary microglia[21] and establishing iMGL banks,[22] generally employing serum/DMSO or serum-replacement mixtures for primary microglia or iMGL. Critically, our protocol applies cryopreservation at the early iHPC stage. This is necessary for efficient mouse engraftment, as others have shown that differentiated or mature iMGL do not engraft efficiently.[9] This approach significantly improves chimeric mouse development by eliminating the logistical requirement to time-match multi-week cell differentiation with the narrow neonatal engraftment window.[6,7,9] We ran phenotypic and functional *in vitro* assays on our generated iMGL and found that cells display typical ramified microglial morphology and express microglial markers including EMR1, CD64, TREM2, CD44, CCR2, CD45, CD14, and CD16, which are also found on primary human microglia.[13]

We confirmed colonization of the murine CNS with human iPSC-derived microglia that resemble their primary human counterparts both phenotypically and functionally. Whole-brain 3D microscopic mapping revealed an increase in chimerism over time, indicating continued expansion of cells *in vivo*. In this process, the amount of CSF1 is determinant in the degree of chimerism, as concluded from observing differences between $CSF1^{HO}$ and $CSF1^{HE}$ animals. While the remainder of this manuscript focusses on brain chimerism, we also observed human cells colonizing the spinal cord, which may be of interest for investigating diseases that present at this level, such as amyotrophic lateral sclerosis (ALS) or other spinal cord pathologies. A phenotypic shift was observed through CyTOF, indicating the maturation of iMGL which has also been reported by others.[20] With up to 80% of all $CD45^{+}$ cells being of mouse origin, this indicates that human cells are replacing their mouse counterparts. The functional capacities of iMGL were confirmed through their evident response to peripheral LPS administration, as well as their capacity to phagocytose zymosan beads. Finally, we observed that the transcriptome of iMGL derived from chimeric mice more closely resembles primary human microglia than *in vitro* cultured iMGL and that the presence of engrafted human cells induces transcriptional changes in the resident cells of the immunodeficient host brain.

We compared head-to-head iMGL generated through our method with a recently published protocol,[7] and found that iMGL adopted the same phenotype and a similar iMGL brain integration profile but with the added practical advantages of our culturing protocol, as outlined above. It must be noted that the cited manuscript achieved an overall higher chimerism average of 32% at 3 weeks, albeit with variation between 20% and 45% and a limited number of replicates per iPSC line shown. The authors report a chimerism of 60%–80% after 2.5 months, levels that are comparable to our results in $CSF1^{HO}$ after 12 weeks. Differences between these studies may be explained by the use of a different mouse strain (MITRG; Jax 017711), in which human CSF1 insertion was performed using different techniques. This may translate into differences in the amount and spatiotemporal expression of the CSF1 transgene—knock-in of the human CSF1 gene for MITRG, versus insertion of the CSF1 gene with its promotor for NSG-CSF1.[23,24] In addition, the difference in chimerism efficiency may be explained by variability across the iPSC lines used in both studies.[7] Both NSG-CSF1 and MITRG are considered extremely immunodeficient models, lacking T, B, and NK cells to minimize graft-versus-host reactions, but differences in their exact genetic background may also contribute to chimerism efficiency and observed phenotypes.

We have used human microglia chimeric mice to gain insights into human microglial responses to various AAV serotypes and how these compare with their murine counterparts. This is particularly important given the heavy reliance on transgenic rodent models in preclinical studies. Our findings indicate that mouse and human microglia show both shared and divergent responses to AAV vectors, with mouse microglia exhibiting stronger activation compared to engrafted iMGLs. This may reflect the lower local abundance of human cells or their limited reception of paracrine cues from surrounding murine cells. While these results suggest potential species-specific differences, the contribution of engraftment-related factors cannot be fully excluded.

Limitations of the study

A limitation of the present study is the occurrence of variability at different experimental levels. These include the spatial variability of human cell integration, needle positioning during intracerebral AAV injections, and other deviations during readouts, such as anatomical sampling differences during tissue sectioning. To minimize these effects, we used mice aged at least 12 weeks, allowing for maximal distribution of human cells across the brain. In addition, stereotaxic procedures were performed using a robotic-controlled drill and injector for adult AAV administration to reduce stereotaxic positioning errors. A stereotaxic atlas

(B) Representative sample displaying the number of unique molecular identifiers (UMIs) counts per spot and the result from Allen brain Atlas registration process.
(C) Expression levels of established brain cell type markers for the exemplary AAV9 1×10^{10} condition are shown.
(D) For the same markers, regional assessment of the spots that detect RNA for the canonical markers is shown.
(E) Correlation matrix of the top genes correlating with RFP expression.
(F) Cell type annotation of the genes from panel E. Allen Brian Atlas abbreviations are in Table S1.

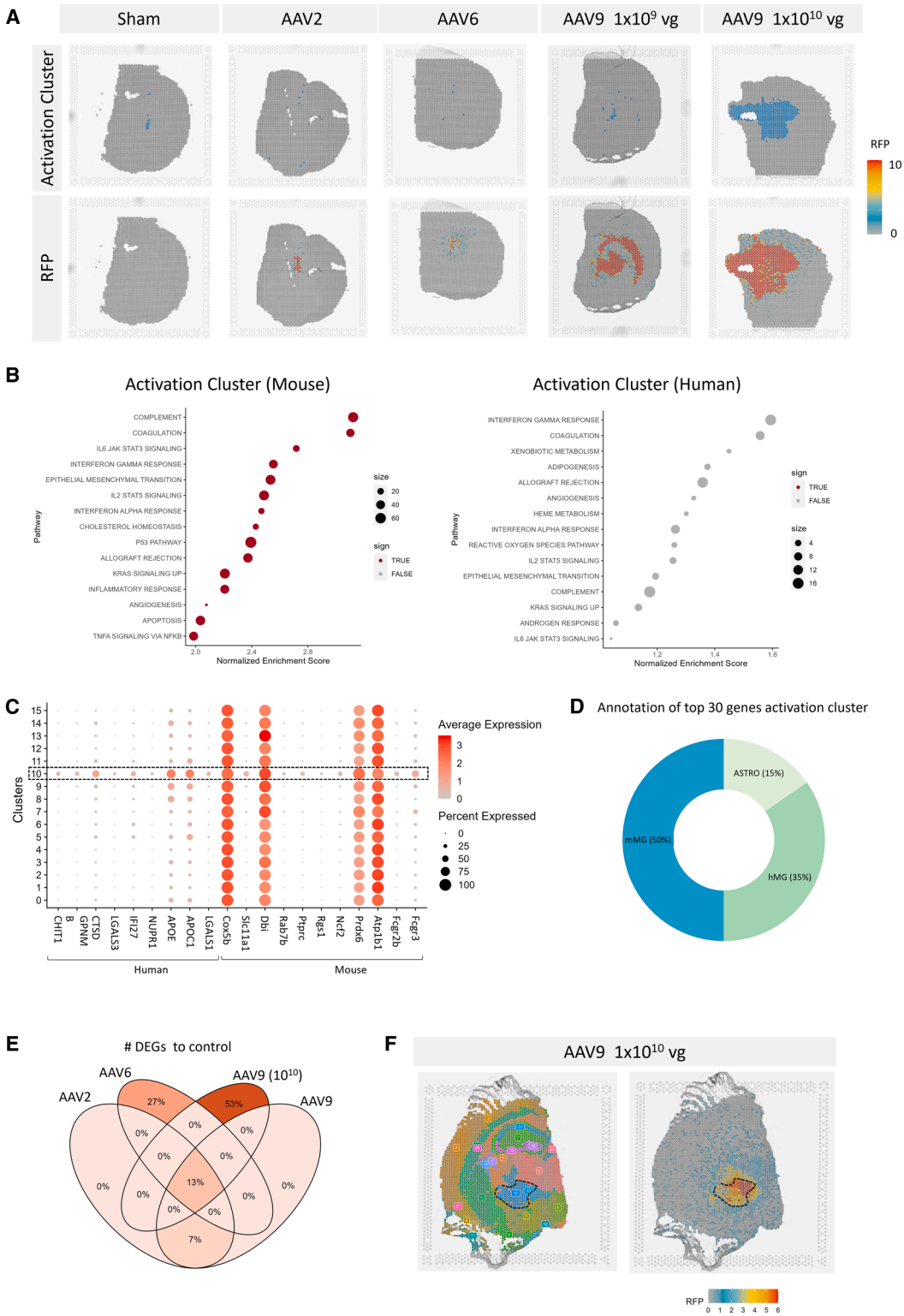

Figure 7. Cluster analysis of AAV serotype responses measured by spatial transcriptomics

(A) Activation cluster projected on exemplary slices for each treatment condition of the experiment, alongside the detected RFP expression pattern.

(B) GO enrichment analysis of mouse and human genes upregulated in the activation clusters.

(legend continued on next page)

was then used when brain section sampling was required, such as for spatial transcriptomics experiments.

We currently use a chimeric model introducing only human microglia into the mouse brain, which allows controlled analysis of microglia-intrinsic responses to AAV. Interactions with murine neurons and glia may not fully reflect human cell-cell communication, and future co-engraftment with additional human neurons and glial cells, such as astrocytes, will help assess how a more human-like cellular environment shapes the brain's immune response.[25] From the same perspective, expanding the engraftment process by introducing peripheral human immune components through peripheral CD34$^+$ cell engraftment would allow dissection of the potential effects of central-peripheral immune crosstalk with circulating immune cells such T, B, NK, and blood-derived myeloid cells. Others have also engrafted iPSC-derived neurons, either directly or via a spheroid intermediary, which allows study of processes involving neuronal networks.[20,26] A key limitation of the chimeric model is that observed differences between human and mouse microglial responses cannot yet be conclusively attributed to species-specific biology. Engraftment density, spatial distribution, and altered interactions with the host environment may influence responses. Follow-up studies using engrafted murine microglia under controlled engraftment conditions will be necessary to distinguish true species-dependent effects from those arising from the transplantation process.

Furthermore, AAV vectors have shown the ability to support long-term transgene expression in the CNS in rodent and non-human primate models.[27] This sustained expression underscores AAV's potential for treating chronic neurological diseases that require sustained gene delivery. However, this prolonged expression also calls for extended evaluations of the brain's response to AAV, which were beyond the scope of this study. Future investigations could uncover additional influencing factors, such as aging, disease progression, and changes in the inflammatory status of cells throughout the disease course.[15]

In conclusion, we established a high-yield protocol for generating iMGLs suitable for creating chimeric mouse brains and used this model to evaluate the effects of different AAV serotypes on both human and mouse brain cells *in vivo*.

RESOURCE AVAILABILITY

Lead contact

Requests for further information should be directed to and will be fulfilled by the lead contact, Jan R. Detrez (jan.detrez@ucb.com).

Materials availability

This manuscript contains no unique reagents or resources.

Data and code availability

- Single-cell RNA sequencing data have been deposited at GEO under accession number GSE312740 and are publicly available as of the date of publication. This paper also analyses existing, publicly available data accessible at GSE137444. Other data, including microscopy, flow cytometry, and spatial transcriptomics data reported in this paper, will be shared by the lead contact upon request.
- This paper does not report original code.
- Any additional information required to reanalyze the data reported in this paper is available from the lead contact upon request.

ACKNOWLEDGMENTS

We thank H. Rhys, E. Sutton, and C. Pang for developing tools for automated CyTOF data pre-processing, as well as A. Bousard, L. François, and B. Van de Sande for their input on single-cell analysis. We also thank T. Patel for his assistance with modeling clinically relevant human AAV doses for mouse studies. This project was supported by joint funding from UCB and the Walloon Region (Belgium) – DGO6 (Convention 7788) from October 2019 to August 2021.

AUTHOR CONTRIBUTIONS

Conceptualization, J.R.D. and I.K.; methodology, J.R.D., C.E., M.P., G.G., J.G., S.C., and P.S.; investigation, J.R.D., C.E., M.P., G.G., J.G., and S.C.; writing—original draft, J.R.D. and I.K.; writing - review and editing, all authors; funding acquisition, I.K.; resources, I.K.; supervision, I.K.

DECLARATION OF INTERESTS

The authors affiliated with UCB may hold stock and shares in the company. C.E. (now at Argenx), M.P. (now at Labcorp Drug Development), and I.K. (now at Genentech) were UCB employees at the time of the study but have since joined other institutions.

STAR★METHODS

Detailed methods are provided in the online version of this paper and include the following:

- KEY RESOURCES TABLE
- EXPERIMENTAL MODEL AND STUDY PARTICIPANT DETAILS
  - NSG mice
  - Generation of human iHPCs
- METHOD DETAILS
  - iHPC differentiation to microglia
  - Human iMGL functional assays
  - Tissue clearing and labeling for light-sheet microscopy and analysis
  - *Ex vivo* tissue processing for CyTOF
  - CyTOF data analysis
  - Single-cell sequencing and analysis
  - Spatial transcriptomics and analysis
  - *Ex vivo* phagocytosis assay and analysis
  - Generation of chimeric mice
  - Systemic LPS administration
  - AAV generation and intra-striatal injections
- QUANTIFICATION AND STATISTICAL ANALYSIS

SUPPLEMENTAL INFORMATION

Supplemental information can be found online at https://doi.org/10.1016/j.crmeth.2026.101362.

(C) Expression levels and percentage of spots expressing the top 20 markers that identify the activation cluster, generated by Seurat FindMarkers, are shown.
(D) Gene annotation of the genes from (C) indicates that the activation cluster is dominated by microglial gene activation.
(E) The number of DEGs within the activation cluster compared to the control group is shown in a Venn diagram.
(F) Cluster analysis performed on the caudal brain region.

Received: October 3, 2025
Revised: December 9, 2025
Accepted: February 19, 2026
Published: March 26, 2026

REFERENCES

1. Bulaklak, K., and Gersbach, C.A. (2020). The once and future gene therapy. Nat. Commun. *11*, 5820. https://doi.org/10.1038/s41467-020-19505-2.
2. Guo, Y., Chen, J., Ji, W., Xu, L., Xie, Y., He, S., Lai, C., Hou, K., Li, Z., Chen, G., and Wu, Z. (2023). High-titer AAV disrupts cerebrovascular integrity and induces lymphocyte infiltration in adult mouse brain. Mol. Ther. Methods Clin. Dev. *31*, 101102. https://doi.org/10.1016/j.omtm.2023.08.021.
3. Costa-Verdera, H., Meneghini, V., Fitzpatrick, Z., Abou Alezz, M., Fabyanic, E., Huang, X., Dzhashiashvili, Y., Ahiya, A., Mangiameli, E., Valeri, E., et al. (2025). AAV vectors trigger DNA damage response-dependent pro-inflammatory signalling in human iPSC-derived CNS models and mouse brain. Nat. Commun. *16*, 3694. https://doi.org/10.1038/s41467-025-58778-3.
4. Chen, Y., and Colonna, M. (2021). Microglia in Alzheimer's disease at single-cell level. Are there common patterns in humans and mice? J. Exp. Med. *218*, e20202717. https://doi.org/10.1084/jem.20202717.
5. Hasselmann, J., and Blurton-Jones, M. (2020). Human iPSC-derived microglia: A growing toolset to study the brain's innate immune cells. Glia *68*, 721–739. https://doi.org/10.1002/glia.23781.
6. Hasselmann, J., Coburn, M.A., England, W., Figueroa Velez, D.X., Kiani Shabestari, S., Tu, C.H., McQuade, A., Kolahdouzan, M., Echeverria, K., Claes, C., et al. (2019). Development of a Chimeric Model to Study and Manipulate Human Microglia In Vivo. Neuron *103*, 1016–1033.e10. https://doi.org/10.1016/j.neuron.2019.07.002.
7. Fattorelli, N., Martinez-Muriana, A., Wolfs, L., Geric, I., De Strooper, B., and Mancuso, R. (2021). Stem-cell-derived human microglia transplanted into mouse brain to study human disease. Nat. Protoc. *16*, 1013–1033. https://doi.org/10.1038/s41596-020-00447-4.
8. Mancuso, R., Van Den Daele, J., Fattorelli, N., Wolfs, L., Balusu, S., Burton, O., Liston, A., Sierksma, A., Fourne, Y., Poovathingal, S., et al. (2019). Stem-cell-derived human microglia transplanted in mouse brain to study human disease. Nat. Neurosci. *22*, 2111–2116. https://doi.org/10.1038/s41593-019-0525-x.
9. Svoboda, D.S., Barrasa, M.I., Shu, J., Rietjens, R., Zhang, S., Mitalipova, M., Berube, P., Fu, D., Shultz, L.D., Bell, G.W., et al. (2019). Human iPSC-Derived Microglia Assume a Primary Microglia-like State after Transplantation into the Neonatal Mouse Brain (Proceedings of the National Academy of Sciences). https://doi.org/10.1073/pnas.1913541116.
10. Xu, R., Li, X., Boreland, A.J., Posyton, A., Kwan, K., Hart, R.P., and Jiang, P. (2020). Human iPSC-derived mature microglia retain their identity and functionally integrate in the chimeric mouse brain. Nat. Commun. *11*, 1577. https://doi.org/10.1038/s41467-020-15411-9.
11. Honda, S., Sasaki, Y., Ohsawa, K., Imai, Y., Nakamura, Y., Inoue, K., and Kohsaka, S. (2001). Extracellular ATP or ADP Induce Chemotaxis of Cultured Microglia through Gi/o-Coupled P2Y Receptors. J. Neurosci. *21*, 1975–1982. https://doi.org/10.1523/JNEUROSCI.21-06-01975.2001.
12. Marsh, S.E., Walker, A.J., Kamath, T., Dissing-Olesen, L., Hammond, T.R., de Soysa, T.Y., Young, A.M.H., Murphy, S., Abdulraouf, A., Nadaf, N., et al. (2022). Dissection of artifactual and confounding glial signatures by single-cell sequencing of mouse and human brain. Nat. Neurosci. *25*, 306–316. https://doi.org/10.1038/s41593-022-01022-8.
13. Böttcher, C., Schlickeiser, S., Sneeboer, M.A.M., Kunkel, D., Knop, A., Paza, E., Fidzinski, P., Kraus, L., Snijders, G.J.L., Kahn, R.S., et al. (2019). Human microglia regional heterogeneity and phenotypes determined by multiplexed single-cell mass cytometry. Nat. Neurosci. *22*, 78–90. https://doi.org/10.1038/s41593-018-0290-2.
14. Schedlowski, M., Engler, H., and Grigoleit, J.-S. (2014). Endotoxin-induced experimental systemic inflammation in humans: A model to disentangle immune-to-brain communication. Brain Behav. Immun. *35*, 1–8. https://doi.org/10.1016/j.bbi.2013.09.015.
15. Seok, J., Warren, H.S., Cuenca, A.G., Mindrinos, M.N., Baker, H.V., Xu, W., Richards, D.R., McDonald-Smith, G.P., Gao, H., Hennessy, L., et al. (2013). Genomic responses in mouse models poorly mimic human inflammatory diseases. Proc. Natl. Acad. Sci. USA *110*, 3507–3512. https://doi.org/10.1073/pnas.1222878110.
16. Crowley, M.T., Costello, P.S., Fitzer-Attas, C.J., Turner, M., Meng, F., Lowell, C., Tybulewicz, V.L., and DeFranco, A.L. (1997). A Critical Role for Syk in Signal Transduction and Phagocytosis Mediated by Fcγ Receptors on Macrophages. J. Exp. Med. *186*, 1027–1039.
17. Stone, D., Aubert, M., and Jerome, K.R. (2023). Breaching the blood-brain barrier: AAV triggers dose-dependent toxicity in the brain. Mol. Ther. Methods Clin. Dev. *31*, 101105. https://doi.org/10.1016/j.omtm.2023.09.001.
18. Maurya, S., Sarangi, P., and Jayandharan, G.R. (2022). Safety of Adeno-associated virus-based vector-mediated gene therapy—impact of vector dose. Cancer Gene Ther. *29*, 1305–1306. https://doi.org/10.1038/s41417-021-00413-6.
19. Bali, B., Gruber-Dujardin, E., Kusch, K., Rankovic, V., and Moser, T. (2022). Analyzing efficacy, stability, and safety of AAV-mediated optogenetic hearing restoration in mice. Life Sci. Alliance *5*, e202101338. https://doi.org/10.26508/lsa.202101338.
20. Schafer, S.T., Mansour, A.A., Schlachetzki, J.C.M., Pena, M., Ghassemzadeh, S., Mitchell, L., Mar, A., Quang, D., Stumpf, S., Ortiz, I.S., et al. (2023). An in vivo neuroimmune organoid model to study human microglia phenotypes. Cell *186*, 2111–2126.e20. https://doi.org/10.1016/j.cell.2023.04.022.
21. Morsey, B., Niu, M., Dyavar, S.R., Fletcher, C.V., Lamberty, B.G., Emanuel, K., Fangmeier, A., and Fox, H.S. (2021). Cryopreservation of microglia enables single-cell RNA sequencing with minimal effects on disease-related gene expression patterns. iScience *24*, 102357. https://doi.org/10.1016/j.isci.2021.102357.
22. Mathews, M., Wißfeld, J., Flitsch, L.J., Shahraz, A., Semkova, V., Breitkreuz, Y., Neumann, H., and Brüstle, O. (2023). Reenacting Neuroectodermal Exposure of Hematopoietic Progenitors Enables Scalable Production of Cryopreservable iPSC-Derived Human Microglia. Stem Cell Rev. Rep. *19*, 455–474. https://doi.org/10.1007/s12015-022-10433-w.
23. Lee, J., Brehm, M.A., Greiner, D., Shultz, L.D., and Kornfeld, H. (2013). Engrafted human cells generate adaptive immune responses to Mycobacterium bovis BCG infection in humanized mice. BMC Immunol. *14*, 53. https://doi.org/10.1186/1471-2172-14-53.
24. Rongvaux, A., Willinger, T., Martinek, J., Strowig, T., Gearty, S.V., Teichmann, L.L., Saito, Y., Marches, F., Halene, S., Palucka, A.K., et al. (2014). Development and function of human innate immune cells in a humanized mouse model. Nat. Biotechnol. *32*, 364–372. https://doi.org/10.1038/nbt.2858.
25. Windrem, M.S., Osipovitch, M., Liu, Z., Bates, J., Chandler-Militello, D., Zou, L., Munir, J., Schanz, S., McCoy, K., Miller, R.H., et al. (2017). Human iPSC Glial Mouse Chimeras Reveal Glial Contributions to Schizophrenia. Cell Stem Cell *21*, 195–208.e6. https://doi.org/10.1016/j.stem.2017.06.012.
26. Espuny-Camacho, I., Michelsen, K.A., Gall, D., Linaro, D., Hasche, A., Bonnefont, J., Bali, C., Orduz, D., Bilheu, A., Herpoel, A., et al. (2013). Pyramidal Neurons Derived from Human Pluripotent Stem Cells Integrate Efficiently into Mouse Brain Circuits In Vivo. Neuron *77*, 440–456. https://doi.org/10.1016/j.neuron.2012.12.011.
27. Ramsingh, A.I., Gray, S.J., Reilly, A., Koday, M., Bratt, D., Koday, M.T., Munson, P., Murnane, R., Smedley, J., Hu, Y., et al. (2018). Sustained AAV9-mediated expression of a non-self protein in the CNS of non-human primates after immunomodulation. PLoS One *13*, e0198154. https://doi.org/10.1371/journal.pone.0198154.
28. Padmakumar, M., Biesmans, S., Valadas, J.S., Detrez, J.R., Gillet, G., Bresler, P., Clénet, M.-L., and Kadiu, I. (2023). An improved method for large scale generation and high-throughput functional characterization

of human iPSC-derived microglia. Front. Drug Discov. *3*, 1289314. https://doi.org/10.3389/fddsv.2023.1289314.

29. Abud, E.M., Ramirez, R.N., Martinez, E.S., Healy, L.M., Nguyen, C.H.H., Newman, S.A., Yeromin, A.V., Scarfone, V.M., Marsh, S.E., Fimbres, C., et al. (2017). iPSC-Derived Human Microglia-like Cells to Study Neurological Diseases. Neuron *94*, 278–293.e9. https://doi.org/10.1016/j.neuron.2017.03.042.

30. Detrez, J.R., Ben-Nejma, I.R.H., Van Kolen, K., Van Dam, D., De Deyn, P.P., Fransen, E., Verhoye, M., Timmermans, J.P., Nuydens, R., Van der Linden, A., et al. (2020). Progressive tau aggregation does not alter functional brain network connectivity in seeded hTau.P301L mice. Neurobiol. Dis. *143*, 105011. https://doi.org/10.1016/j.nbd.2020.105011.

31. Renier, N., Adams, E.L., Kirst, C., Wu, Z., Azevedo, R., Kohl, J., Autry, A.E., Kadiri, L., Umadevi Venkataraju, K., Zhou, Y., et al. (2016). Mapping of Brain Activity by Automated Volume Analysis of Immediate Early Genes. Cell *165*, 1789–1802. https://doi.org/10.1016/j.cell.2016.05.007.

32. Preibisch, S., Saalfeld, S., and Tomancak, P. (2009). Globally optimal stitching of tiled 3D microscopic image acquisitions. Bioinformatics *25*, 1463–1465. https://doi.org/10.1093/bioinformatics/btp184.

33. Detrez, J.R., Maurin, H., Van Kolen, K., Willems, R., Colombelli, J., Lechat, B., Roucourt, B., Van Leuven, F., Baatout, S., Larsen, P., et al. (2019). Regional vulnerability and spreading of hyperphosphorylated tau in seeded mouse brain. Neurobiol. Dis. *127*, 398–409. https://doi.org/10.1016/j.nbd.2019.03.010.

34. Schindelin, J., Arganda-Carreras, I., Frise, E., Kaynig, V., Longair, M., Pietzsch, T., Preibisch, S., Rueden, C., Saalfeld, S., Schmid, B., et al. (2012). Fiji: an open-source platform for biological-image analysis. Nat. Methods *9*, 676–682. https://doi.org/10.1038/nmeth.2019.

35. Burberry, A., Wells, M.F., Limone, F., Couto, A., Smith, K.S., Keaney, J., Gillet, G., van Gastel, N., Wang, J.Y., Pietilainen, O., et al. (2020). C9orf72 suppresses systemic and neural inflammation induced by gut bacteria. Nature *582*, 89–94. https://doi.org/10.1038/s41586-020-2288-7.

36. Bagwell, C.B., Inokuma, M., Hunsberger, B., Herbert, D., Bray, C., Hill, B., Stelzer, G., Li, S., Kollipara, A., Ornatsky, O., and Baranov, V. (2020). Automated Data Cleanup for Mass Cytometry. Cytometry *97*, 184–198. https://doi.org/10.1002/cyto.a.23926.

37. Ianevski, A., Giri, A.K., and Aittokallio, T. (2022). Fully-automated and ultra-fast cell-type identification using specific marker combinations from single-cell transcriptomic data. Nat. Commun. *13*, 1246. https://doi.org/10.1038/s41467-022-28803-w.

STAR★METHODS

KEY RESOURCES TABLE

REAGENT or RESOURCE	SOURCE	IDENTIFIER
Antibodies		
IBA1 antibody	Wako	019–19741
anti-GFP antibody	Aves	GFP-1010
Goat anti-Rabbit IgG (H + L) Highly Cross-Adsorbed Secondary Antibody, Alexa Fluor 790	ThermoFisher Scientific	A11369
Goat anti-Rabbit IgG (H + L) Highly Cross-Adsorbed Secondary Antibody, Alexa Fluor Plus 647	ThermoFisher Scientific	A32733
Goat anti-Chicken IgY (H + L) Cross-Adsorbed Secondary Antibody, Alexa Fluor Plus 488	ThermoFisher Scientific	A32931
Goat Anti-Chicken IgY H&L (Alexa Fluor 647)	Abcam	ab150171
Ly-6G	Fluidigm	3141008B
Ly-6C	Biolegend	128039
CD4	Fluidigm	3145002B
F4/80	Fluidigm	3146008B
CD11b	Fluidigm	3148003B
CD68	Biolegend	137002
CD3e	Fluidigm	3152004B
CD8a	Fluidigm	3153012B
TER-119	Fluidigm	3154005B
CD11c	Fluidigm	3162017B
CD19	Fluidigm	3166015B
CD335	Fluidigm	3167008B
CD117	Fluidigm	3173004B
CD127	Fluidigm	3175006B
FceRIa	Fluidigm	3176006B
MHC II	Fluidigm	3209006B
CD25	biolegend	101913
Siglec-F	biolegend	155502
CD45	Fluidigm Europe BV	3089005B
RAGE	Abcam	ab228861
Tim-3	BioLegend	345019
TREM2	R&D Systems	MAB17291
CD279 (PD-1)	BioLegend	329941
M6PR	Abcam	ab236067
CD206 (MMR)	BioLegend	141702
HLA-A,B,C	Fluidigm Europe BV	3141010B
TGFBR1	Abcam	ab51871
GM-CSFR/CSF2R	R&D Systems	MAB706
CD83	Biolegend	305302
EMR1	Biorad	MCA2674GA
CD64	Fluidigm Europe BV	3146006B
CD11c	Fluidigm Europe BV	3147008B
CD16	Fluidigm Europe BV	3148004B
CD68	Biolegend	137002

(*Continued on next page*)

Continued

REAGENT or RESOURCE	SOURCE	IDENTIFIER
CD169/SIGLEC	Biolegend	346002
CLEC7A (Dectin-1)	Biolegend	355402
CD3e	Fluidigm Europe BV	3152004B
CD192 (CCR2)	Fluidigm Europe BV	3153023B
CD45	Fluidigm Europe BV	3154001B
CD36	Fluidigm Europe BV	3155012B
CD86	Fluidigm Europe BV	3156008B
CD284 (TLR4)	Fluidigm Europe BV	3158024B
CD115/CSF1R	R&D Systems	MAB329
CD80	Fluidigm Europe BV	3161023B
CD95	Fluidigm Europe BV	3162038B
CD172a/b (SIRPa/b)	Fluidigm Europe BV	3163017B
CX3CR1	Fluidigm Europe BV	3164023B
CD40	Fluidigm Europe BV	3165005B
CD204/MSR1	biolegend	371902
CD11b	Fluidigm Europe BV	3167011B
CD206 (MMR)	Fluidigm Europe BV	3168008B
CD33	Fluidigm Europe BV	3169010B
C3aR	Biolegend	345802
CD68	Fluidigm Europe BV	3171011B
CX3CR1	Fluidigm Europe BV	3172017B
HLA-DR	Fluidigm Europe BV	3173005B
I-A/I-E (MHCII)	Fluidigm Europe BV	3174003B
CD14	Fluidigm Europe BV	3175015B
CD282 (TLR2)	Fluidigm Europe BV	3176021B
CD274/PD-L1 (MIH1)	Fluidigm Europe BV	3209014B
Bacterial and virus strains		
AAV6-mAIF1-RFP	Vector Biolabs	Custom order
AAV2-CAG-RFP	Vector Biolabs	Custom order
AAV9-CAG-RFP	Vector Biolabs	Custom order
Chemicals, peptides, and recombinant proteins		
Anti-adherence rinsing solution	Stem Cell Technologies	07010
Gibco DPBS, no calcium, no magnesium	ThermoFisher Scientific	14190250
Accutase solution	Merck	A6964
Matrigel Growth factor reduced, phenol red-free, *LDEV-free	Corning	356231
Laminin from Engelbreth-Holm-Swarm murine sarcoma basement membrane	Merck	L2020
Essential 8 Flex Medium Kit	ThermoFisher Scientific	A2858501
IMDM medium	ThermoFisher Scientific	21980032
Ham's F-12 Nutrient Mix	ThermoFisher Scientific	11765054
Phenol-free DMEM/F12 medium	ThermoFisher Scientific	11039021
Insulin-Transferrin-Selenium-Ethanolamine (ITS-X)	ThermoFischer Scientific	51500056
Insulin-Transferrin-Selenium (ITS-G)	ThermoFischer Scientific	41400045
L-Ascorbic acid 2-phosphate sesquimagnesium salt hydrate	Merck	A8960-5G
1-Thioglycerol	Merck	M-1753-100ML
Poly(vinyl alcohol)	Merck	P8136-250G
GlutaMAX Supplement	ThermoFisher Scientific	35050061

(*Continued on next page*)

Continued

REAGENT or RESOURCE	SOURCE	IDENTIFIER
Chemically-defined lipid concentrate	ThermoFisher Scientific	11905031
MEM Non-Essential Amino Acids Solution	ThermoFisher Scientific	11140035
N2 supplements	ThermoFisher Scientific	17502048
B27 supplements	ThermoFisher Scientific	17504044
Insulin human	Merck	I2643-50mG
Rho kinase inhibitor (Y-27632 dihydrochloride)	Abcam	ab120129
Recombinant Human IL-3	Peprotech	200–03
Recombinant Human IL-6	Peprotech	200–06
C-Kit Ligand (SCF) Recombinant Human Protein	ThermoFisher Scientific	PHC2115
Lithium chloride solution	Merck	L7026-100ML
FGF-Basic (AA 1–155) Recombinant Human Protein	ThermoFisher Scientific	PHG0266
BMP4 Recombinant Human Protein	ThermoFisher Scientific	PHC9534
Activin A Recombinant Human Protein	ThermoFisher Scientific	PHC9564
Recombinant Human VEGF 165	Peprotech	100–20
Thrombopoietin (TPO) Recombinant Human Protein	ThermoFisher Scientific	PHC9514
Recombinant Human M-CSF	PeproTech	300–25
Human TGF-β1	PeproTech	100–21
Recombinant Human IL-34	PeproTech	200–34
DMEM-F12	ThermoFisher Scientific	11320033
mTeSR™ Plus medium	Stemcell Technologies	05825
CryoStor CS10	Stemcell Technologies	07959
pHrodo Red Zymosan Bioparticles	Invitrogen	P35364
Cytochalasin D	Merck	C8273-1MG
Adenosine 5′-diphosphate sodium salt	Sigma-Aldrich	A2754-100MG
PSB 0739	Tocris	3983
liposaccharide (LPS)	Sigma	L5024-10MG
Heparin	Sigma	H3393-50KU
Pluroni F-68 Non-ionic Surfactant (100X)	Thermofisher	24040032
ProLong™ Gold Antifade Mountant	ThermoFisher	P36930
DMSO	ThermoFisher Scientific	D12345
Normal Goat Serum	Abcam	ab7481
Triton X-100	VWR	437002A
Paraformaldehyde, 4% in PBS	alfa aesar	J19943
Dibenzylether	Sigma-Aldrich	108014-1KG
Dichloromethane	Carlroth	8424.4
Methanol, 2,5L	VWR	20847307
eBioscience 1X RBC Lysis Buffer	ThermoFisher Scientific	00-4333-57
Percoll PLUS	Sigma	E0414-1L
Maxpar Cell Staining Buffer	Fluidigm	201068
Pierce 16% Formaldehyde (w/v), Methanol-free	ThermoFisher	28908
Maxpar Cell Acquisition Solution	Fluidigm	201237
Maxpar EQ Four Element Calibration Beads	Fluidigm	201078
autoMACS Running Buffer – MACS Separation Buffer	Miltenyi Biotech	130-091-221
Actinomycin D	Sigma	A1410
Triptolide	Sigma	T3652
Anisomycin	Sigma	A9789
1X HBSS	Thermofisher	14175053

(*Continued on next page*)

Continued

REAGENT or RESOURCE	SOURCE	IDENTIFIER
Myelin Removal Beads II, Human, Mouse, Rat	Miltenyi	130-096-733
BSA UltraPure	ThermoFisher	AM2618
DTT	Teknova	D9750
recombinant RNAse inhibitor	TakaraBio	2313B
Critical commercial assays		
Papain Dissociation Kit	Worthington	LK003153
Deposited data		
Single-cell RNA sequencing data	This paper	GSE312740
human primary microglia data obtained from cortical surgical resections	GEO	GSE137444
Experimental models: Cell lines		
ASE-9109 iPSC line	Applied StemCell, Inc	ASE-9109
Experimental models: Organisms/strains		
NSG-CSF1 mice	Jax	028654
Software and algorithms		
FIJI (ImageJ v.1.54j)	Schindelin et al.[28]	https://imagej.net/software/fiji
cellranger v.7.1	10X	https://www.10xgenomics.com/support/software/cell-ranger/downloads
spaceranger v.2.0.0	10X	https://www.10xgenomics.com/support/software/cell-ranger/downloads
Seurat v5.0.3	Satijalab	Abud et al.[29]
DESeq2	Simon Anders	Detrez et al.[30]
Other		
Falcon 6-well Clear Flat Bottom TC-treated Multiwell Cell Culture Plate	Corning	353046
AggreWell 400 6-well plates	Stem Cell Technologies	34425
Corning BioCoat Poly-D-Lysine 6-well Clear Flat Bottom TC-treated Multiwell Plate	Corning	356413
Cell scraper	Merck	CLS3008
37 μm reversible cell strainer	Stem Cell Technologies	27250
Countess II Automated Cell Counter	ThermoFisher Scientific	AMQAX1000
Nalgene Mr. Frosty freezing container	Merck	C1562-1EA
T175 Nunc Poly-D-Lysine or Collagen I Coated EasYFlasks	Thermofisher	132705
PDL-precoated clear bottom 384-well plate	Corning	354663
IncuCyte S3	Sartorius	Incucyte S3
IncuCyte ClearView 96-Well Cell Migration Plate	Sartorius	4582
Mouse and Neonates Adaptor	Stoelting	51625
Hamilton 32G syringe (Angle: 30, Needle Length: 10 mm, Point Style: 4)	Hamilton	7803–04
Play-Doh Clay	Hasbro	Play-Doh
Robot Stereotaxic	Neurostar	Robot Stereotaxic
Animal heater (Fisherbrand Isotemp Digital Dry Baths/Block Heaters)	Fisher Scientific	88-860-021
Digital Heating Shaking Drybath	Fisher Scientific	88-880-028
Vibratome	Leica	VT 1200 S
Incubation chambers	Harvard Apparatus	Prechamber BSC-PC
Confocal microscope	Zeiss	LSM880
40 μm Nylon Cell Strainer	Falcon	352340
96-well plate, PP, V-bottom	Corning	CLS3363

(*Continued on next page*)

Continued

REAGENT or RESOURCE	SOURCE	IDENTIFIER
Cell-ID™ Intercalator-Ir—500 μM	Fluidigm	201192B
5mL polypropylene FACS tubes	Corning	352063
5mL tubes with cell-strainer (35μM) cap, PS	Corning	352235

EXPERIMENTAL MODEL AND STUDY PARTICIPANT DETAILS

NSG mice

NSG-CSF1$^{+/-}$ mice, expressing human CSF1 on a NOD/ShiLtJ background with severe combined immune deficiency (Prkdc^{scid}) and a targeted knockout of the IL2 receptor common gamma chain allele (IL2rg^{null})[23] were licensed from Jackson Laboratories (USA). Mice were mated for 72 h and pregnant dams were single-housed, and litters housed by gender after weaning. Prior to engraftment studies offspring (NSG-CSF1$^{+/+}$, NSG-CSF1$^{+/-}$, NSG-CSF1$^{-/-}$) were genotyped by qPCR at UCB and at Charles River (France). Mice were maintained on 12/12 dark/light cycle, at 20°C–24°C and 45–65% humidity with food and water provided *ad libitum*. For all studies, pups were randomised across treatment groups and all studies/readouts were blinded.

Generation of human iHPCs

We have used two iPSC and iMGL generation protocols in this paper. We have used our in-house iPSC culturing detailed below for all the data in this paper,[28] except for studies where we made a comparison to an alternative iMGL generation protocol.[8] For this alternative protocol, we followed iMGL generation exactly as outlined in the cited paper and we provided microscopic images that serve as quality control steps during the protocol progression (Figure S1).

ASE-9109 iPSCs were purchased from a commercial source. Cells were maintained and differentiated in culture in absence of antibiotics or antimitotic agents. iPSCs were edited to express green-fluorescent protein (GFP) reporter under control of the IBA-1 promoter by CRISPR/Cas9 technology at Applied StemCell (ASE-9109-GFP). Maintenance and differentiation of the iPSC line to generate microglia was done according to a modified version of a published protocol.[29] iPSC lines were thawed and cultured in 6-well plates or T225 flasks in mTeSR Plus medium supplemented with Rho kinase inhibitor for the first 24 h. Cells were maintained in feeder-free conditions on Matrigel with medium changes every other day in a humidified incubator (5% CO_2 at 37°C). Passaging was performed with room temperature Accutase for 3–5 min until cells visually detached, followed by inactivation with medium, gentle detachment by a cell scraper, and centrifugation at 300*g* for 5 min. Complete E8 medium was introduced after the last passage, before harvesting in Accutase and up to embryoid body formation stage.

Embryoid body formation was induced by harvesting iPSCs with Accutase, followed by resuspension in induced hematopoietic progenitors (iHPC) base medium, i.e., Iscove's Modified Dulbecco's medium (IMDM; 0.5X), F12 medium (0.5X), Glutamax (1X), chemically-defined lipid concentrate (1X), MEM non-essential amino acids (MEM NEAA; 1X), insulin-transferrin-selenium-ethanolamine (ITS-X; 2%), l-ascorbic 2-phosphate (64 μg/mL), monothioglycerol (400 μm), poly-vinyl-alcohol (PVA; 10μg/ml). AggreWell 400 plates were pre-treated with anti-adherence solution by centrifuging the solution in the plates at 1300 g for 5 min following a wash with 1X PBS. Cells were seeded in AggreWell 400 plates at different densities (0.50×10^6, 0.75×10^6, 1.00×10^6 and 1.25×10^6 per well) to control for variability in cell counting. Plates were centrifuged at 100 xg for 3 min to capture cells in the microwells. Induced hematopoietic progenitor cell (iHPC) base medium was supplemented with Rho kinase inhibitor (10 μm) to support embryoid body formation.

After 24 h, T225 flasks were pre-treated with anti-adherence solution for 10 min and washed with 1X PBS and used for the remainder of the protocol. Embryoid bodies were aspirated from the AggreWell 400 plates and seeded in T225 in iHPC base medium supplemented with FGF2 (50 ng/mL), BMP4 (50 ng/mL), Activin-A (12.5 ng/mL), Rho kinase inhibitor (1 μm), Lithium chloride (2 mM). The day of seeding is marked as d 0 in culture, and flasks were placed for 48 h in hypoxic cell culture conditions (5% O_2, 5% CO_2, 37°C). On d 2, embryoid bodies were aspirated and filtered through a 37 μm reversible cell strainer to be transferred to a new T225 with iHPC base medium supplemented with FGF2 (50 ng/mL), VEGF (50 ng/mL), which was placed for 48 h in hypoxic cell culture conditions. On day 4, embryoid bodies were aspirated and filtered through a 37 μm reversible cell strainer and transferred to a new T225 with iHPC base medium supplemented with FGF2 (50 ng/mL), VEGF (50 ng/mL), TPO (50 ng/mL), SCF (10 ng/mL), IL-3 (10 ng/mL), IL-6 (50 ng/mL) under normoxic conditions. On d 6 flasks were supplemented with d 4 medium, during which iHPC cells started to emerge in the flasks. Embryoid bodies were subsequently fed with d 4 medium every 2–3 days, and iHPCs were harvested at d 14 and d 20 by filtration through a 37 μm reversible cell strainer. Embryoid bodies were collected from the strainer and plated in new T225 for additional iHPCs generation. iHPC were collected, centrifuged at 300 g for 5 min before resuspension in 4°C CryoStor10 at 2-20 $\times 10^6$/mL per cryovial depending on the downstream applications. Cryovials were placed in Mr. Frosty containers containing isopropanol and placed in a −80°C freezer for 24 h followed by cryostorage.

METHOD DETAILS

iHPC differentiation to microglia

Crypreserved iHPCs were thawed and supplemented with d 4 medium supplemented with Rho kinase inhibitor (10 μm). Cells were centrifuged at 300 g for 5 min before resuspension in fresh d 4 medium. Cells were counted and depending on the study seeded in poly-D-lysine T175 at 9.210 $\times$ ^{6}/flask in 40 mL medium for transplantation studies, or 6-well plates at 0.400–0.500 $\times$ 10^{6}/well in 2 mL medium for *in vitro* assays. All culture dishes were pre-coated with laminin (20 μg/ml for 4 h). After 24 h, cells were harvested and centrifuged at 300 g for 5 min for a full medium exchange. To induce differentiation into microglial like cells (iMGL) cells were maintained in phenol-free DMEM/F12 medium (1X), Insulin-Transferrin-Selenium (2%), B27 (1X), N2 (1X), Glutamax (1X), MEM NEAA (1X), Monothioglycerol (200 μM), Insulin human (5 μg/mL). iMGL differentiation medium was supplemented with M-CSF (25 ng/mL), TGF-β1 (50 ng/mL), IL-34 (100 ng/mL). For *in vitro* studies, cells were differentiated for 14 days with partial medium exchanges every 2-3 days to generate mature iMGLs. For transplantation studies, cells were harvested 2–3 days after thawing to generate iMGL progenitors. For these studies, cells were harvested using 37°C sterile 1 XPBS, centrifuged at 300 g for 5 min, and resuspended in appropriate media volumes for each functional assay.

Human iMGL functional assays

After 14 days in culture, cells were harvested and centrifuged at 200 g for 5 min. For the phagocytosis assays, 5000 cells/well were plated in poly-D-lysine (PDL) and laminin (20 μg/mL for 4 h) precoated 384-well plates in iMGL differentiation medium supplemented as described above. Cytochalasin D, a positive control for blockade of phagocytic activity, was added 1 h after seeding at different concentrations (1.25, 2.5, 5 and 10 μM) to specific wells, and fluorescently conjugated Zymosan beads (0.500 μg/well) were added after an additional 1 h. Time-lapse imaging was performed at 37 C and 5% CO_2 every 30 min for 24 h in an IncuCyte S3 imaging instrument. Each condition was replicated in 4 different wells (n = 4). For the chemotaxis assay, 2500 cells/well were plated in the top compartment of a 96-well transwell cell migration plate. A P2Y12 receptor antagonist PSB 0739 was added into 4 replicate positive control wells at 12.5 μM, 25 μM and 50 μM immediately after seeding. Cells were allowed to settle for 15 min followed by addition of 150 μL (100 μM) of the chemoattractant adenosine diphosphate (ADP) to the bottom compartment at 100 μM. The 96-well plate insert containing cells exposed to various treatments was inserted in the bottom compartment containing the chemoattractant and incubated at 37°C at 5% CO_2 for an additional 15 min prior to time lapse imaging in the IncuCyte S3 every 90 min for 24 h.

In vitro LPS treatment was performed by splitting a pool of cells over PDL and laminin (20 μg/mL for 4 h) precoated 6-well plates in iMGL differentiation base medium with the peptide supplements indicated earlier. After cells settled for 1 h, treatments were applied by adding prediluted compounds to achieve a final concentration of 0.3, 3 and 30 μg/mL in LPS in PBS after adding to the cell medium. A negative control (medium only) was included. Cells were harvested using 37°C PBS and centrifugation at 300*g* for 5 min and transferred in a V-bottom 96-well plate and processed as described in the Cytometry by time of flight (CyTOF) processing section.

Tissue clearing and labeling for light-sheet microscopy and analysis

Mice were transcardially perfused with 1X PBS as described above. One brain hemisphere and spinal cords were drop-fixed overnight in 4% PFA at 4°C, followed by a PBS wash (3 $\times$ 15 min) and storage in PBS with 0.1% NaN_3 at 4°C until further processing. Fluorescent labeling and clearing of samples was performed using the iDISCO+ protocol as previously described.[30,31] Brains were stained with antibodies Iba1, targeting mouse and human microglia, and anti-GFP, staining human microglia, for 2 weeks at 37°C, followed by secondaries Alexa Fluor 790 conjugated goat-*anti*-rabbit antibody and Alexa Fluor 647 goat Anti-Chicken at 37°C for 1 w.

Cleared samples were acquired with an Ultramicroscope Blaze, equipped with an MI PLAN 4X/0.35 objective lens and DBE-corrected dipping cap. Images were recorded with an Andor *Neo* sCMOS camera at a total magnification of 4X and a z-step of 10 μm resulting in 1.62 μm^2 $\times$ 10 μm voxels. Tiled images from the left and right light sheets were merged on-the-fly with a linear blending algorithm, and by custom-made stitching script in ImageJ based on a published stitching plugin.[32] A 488 nm, 561 nm, 640 nm and 785 nm laser with a 525/50 nm, 620/60 nm, 680/30 nm and 845/55m emission filter were used.

Whole-brain microscopy images were analyzed using a fully automated method as previously described.[33] Briefly, the autofluorescence channel was automatically aligned to a 3D light sheet reference brain atlas, and the resulting transformation vector set was used for regional analysis of the detection signal of interest, i.e., IBA1 human and mouse microglia staining or GFP cell staining for differentiating the human microglial population. Cell detection was done in an automated way by use of trivial pre- and postprocessing tools (e.g., background subtraction, median filtering, thresholding, particle size filtering) in ImageJ,[34] applying the same settings for all samples within one experiment. The total number of detected voxels for a given brain region was calculated and expressed relative to the brain region volume (volume %). A custom regional analysis approach was made for spinal cord segmentation (Figure S4C). After binarizing the spinal cord autofluorescence, a skeleton was created that was used for tracing the center line of the spinal cord with a segmented line. This line was then fit with a spline that was used to divide the spinal cord in 30 segments based on their known proportional sizes. Cell detection was done as described previously, and the detected voxels for a given spinal cord region was calculated and expressed relative to region volume (volume %).

Ex vivo tissue processing for CyTOF

Chimeric mice at various ages were anesthetized and transcardially perfused as described above. Post anesthesia and prior to the perfusion peripheral blood samples were collected by cardiac puncture into heparin/EDTA blood collection tubes and placed on wet ice for further processing. One brain hemisphere was collected in 1X HBSS and kept on wet ice for further processing. Brain dissociations were performed as previously described.[35] Briefly, brains were dissociated using a papain-based dissociation kit at 37 C and 5% CO_2 for 30 min (according to the manufacturer's instructions) with gentle triturations using 10 and 5 mL serological pipettes in 10 min intervals. Papain was inhibited by albumin-ovomucoid solution mixed with DNAse. Single cell suspensions were filtered through a 40 μm cell strainer and resuspended in 30% Percoll in 1x HBSS and centrifuged at room temperature for 15 min at 500 g with no brake to remove the top myelin layer. Spleens were homogenized by mechanical dissociation followed by red blood cell removal using RBC lysis buffer for 10 min and filtered through a 40 μm cell strainer. Peripheral blood samples were centrifuged for 10 min at 300 g with no brake. The buffy coats were collected and resuspended in RBC lysis buffer for 10 min to remove erythrocytes. All cell pellets were washed with autoMACS running buffer.

Antibodies in the CyTOF panel were obtained either pre-conjugated to metal isotope or in CyTOF-ready formats from various suppliers and conjugated in-house using the Maxpar Antibody Labeling Kit following manufacturer's instructions.

Cell pellets from each mouse were washed with Maxpar Cell Staining buffer and then plated in v-bottom 96-well plates used for staining and incubated with a cocktail of metal-tagged antibodies for 45 min at 4°C followed by 15 min at room temperature. After incubation, cells were washed 3 times by centrifugation at 300*g*, 4C in Maxpar Cell Staining buffer and fixed in 4% PFA in 1X PBS at 4°C.

One day prior to acquisition, fixed cells were incubated with the Maxpar $^{191/193}$Ir DNA Intercalator (50 nM) diluted in 4% PFA in PBS at 4°C overnight. Cells were washed twice in Maxpar H_2O and centrifuged at 800 g. Cells were resuspended in EQ Four Element Calibration beads diluted in Maxpar Cell Acquisition Solution (1:4), filtered through a 40 μm cell strainer and acquired on a Helios mass cytometer. Samples were acquired at an event rate of maximum 500 events/s with a detection limit at 100.000 events.

CyTOF data analysis

Raw data was normalised and converted to fcs format in CyTOF Software. All down-stream processing was done in R (S4A). Data was pre-processed based on conventional quality control steps (e.g., DNA intensity, event length, bead exclusion), but also included additional Gaussian parameters that are extracted from the individual pulses.[36] An automated batch processing Shiny app was developed for EQ bead removal (*flowStats::rangeGate*) and for determining a Gaussian cut off based the width, residual, center, offset and DNA intensity parameters (*flowStats::curv1filter*). Visual verification of the automated thresholding was performed, and detection parameters were adjusted if needed. Filtered data was gated to isolate cell populations by manual drawing of a region of interest on a scatterplot (*CytoExploreR*), or by subsetting data after cluster analysis (*Spectre::run.flowsom*). For the cluster analysis, the data was subsampled to have an equal of 4000 cells per study group. A relevant number of clusters was chosen based on the biological context. Small clusters (containing less than 1% of all cells) were considered not relevant and were shown in gray and labeled as NA. Data was represented as a UMAP, heatmap, bar and density plots (*Spectre; ggplot2*).

Single-cell sequencing and analysis

Considering microglia are particularly sensitive to acquiring artifactual activation signatures resulting from tissue processing prior to single cell sequencing,[1] we investigated whether usage of transcriptional inhibitors (actinomycin D, triptolide, anisomycin) can mitigate this issue (Figure S5A). We first compared head-to-head a protocol with and without the use of these inhibitors using two brain hemispheres derived from the same chimeric mouse, together with additional hemispheres from other mice. Isolating human and mouse microglia on a UMAP plot, the sample that was treated with such inhibitors was shifted from non-treated controls (Figures S5A, S5B). We found that this phenotypic shift corresponds to expression of immediate-early genes (Fos, Jun), cellular stress (Dusp) among others (Figure S5C). This was also apparent from the expression levels of these genes (Figure S5D). Following this experiment, we continued the usage of these inhibitors for the single cell studies.

Mice were perfused with ice-cold 1X HBSS with 10 U/ml heparin, together with transcriptional inhibitors were added actinomycin D (5 μg/mL), triptolide (10 μM) as was done in other studies.[12] Samples were collected on ice in 1X HBSS that contained anisomycin (27.1 μg/mL) as a third transcription inhibitor, as well as RNase Inhibitor (0.2 U/μl) and DTT (1 mM). All compounds were used in all subsequent solutions at the same concentrations, together with and sample were kept at 4°C throughout the process. Brain dissociations were performed based on an adapted protocol previously described for CyTOF tissue processing. Brains were dissociated using a papain-based dissociation kit at 37 C and 5% CO_2 for 30 min (according to the manufacturer's instructions) with gentle triturations using 10 and 5 mL serological pipettes in 10 min intervals. Papain was inhibited by albumin-ovomucoid solution mixed with DNAse. Single cell suspensions were filtered through a 40 μm cell strainer and resuspended in Myelin Removal Beads II solution according to manufacturer's instructions. Dynamag magnets were used to remove myelin from the solution. For cell culture cells, cells were detached using 37°C PBS and a cell scraper. After passing through a 40 μm cell strainer, cell suspensions were spun at 300 g for 5 min and resuspended in 1X PBS with 0.1% before loading on the Chromium device.

10X single-cell libraries were prepared following the manufacturer's guidelines per mouse, without pooling. As 10X chips are limited to 8 samples per run, some experiments were run in multiple processing batches. Sequencing was done on an Illumina NovaSeq6000, targeting 10K cells with 35M reads per cell.

Raw bcl files were converted to FASTQ by 10X's tool *cellranger mkfastq v.7.1*, Followed by creation of gene expression matrices by *cellranger count v.7.1* using the provided merged *GRCh38* and *mm10* genome. Samples were pre-filtered during import in R with *Seurat::CreateSeuratObject* set to filter keeping a minimum of 10 cells per gene and 200 genes per cell. Following visualisation of the distribution of features, samples were additionally filtered, keeping cells with more than 2000 genes per cell and less than 10% mitochondrial genes. Normalisation was done using *Seurat::SCTransform* using *glmGamPoi*, regressing out the cell cycle gene score, the percentage of mitochondrial genes, the processing batch, number of features, and the original identity. Multi-resolution clustering was performed initially, and an appropriate resolution was chosen based on its alignment with the biology. A processing batch effect was observed between subsequent 10X chip runs, and *harmony:: RunHarmony* was performed, effectively mering separated clusters. Automated cluster annotation was performed by ScType,[37] followed by manual curation of the clusters based on canonical marker expression. Cluster pseudo-bulk differential gene expression (DEG) analysis was done by aggregating the count matrix to sample levels, followed by re-clustering of the raw count matrix per cluster and *DESeq2::DESeq* analysis and visualisation in volcano plots with cut-offs for false discovery rate (FDR) corrected *p*-values at 0.05 and an absolute log10-fold change (FC) at 1. All figures were generated by pseudo-bulk clustering, unless indicated otherwise. Gene enrichment was done through fgseafgsea, using GO database *m5.all.v2022.1.Mm*.

We have compared the identity of our iMGL to primary human microglia, which were derived from an online repository (GSE137444 [8]). After reading and filtering datasets as mentioned above, datasets were integrated by *harmony::RunHarmony*, followed by clustering and UMAP representation of the data.

Spatial transcriptomics and analysis

Spatial transcriptomics was performed following the fresh frozen protocol Visium Spatial Gene Expression from 10X. In brief, mice were perfused with ice-cold 1X HBSS with 10 U/ml heparin, and brains were snap-frozen in OCT compound in isopentane and stored at −80°C. Tissue slices were generated at 14 μm and placed on the Visium slide, after which H&E staining and imaging was conducted. Tissues were permeabilised to release the RNA on the capture probes, and the library was generated and sequenced with 50.000 read pairs per capture spot on an Illumina NovaSeq6000.

For 10X Visium analysis, raw bcl files were converted to FASTQ by 10X's tool *cellranger mkfastq v.7.1*, Followed by creation of gene expression matrices by *spaceranger count v.2.0.0* using the provided merged *GRCh38* and *mm10* genome that was modified to also detect green fluorescent protein (GFP) and red fluorescent protein (RFP) sequences. Anatomical annotation was done by registering the Allen Brain Atlas (ABA) labels on the H&E image in FIJI using landmark detection followed by an affine transformation using the *Landmark Correspondence* FIJI plugin.[34] Samples were read in R with *Seurat::Load10X_Spatial* and annotation and metadata was added, followed by normalisation using *Seurat::SCTransform*. Data clustering, visualisation and DEG analysis was done with tools from the same package, and as described for single-cell analysis above.

Ex vivo phagocytosis assay and analysis

Brain and spinal cord were obtained as described earlier, and were quickly transferred for generation of 300 μm coronal sections using a vibratome in ice-cold freshly prepared carbogen (95% CO_2,5% O_2)-bubbled artificial cerebrospinal fluid solution (aCSF) consisting of 126 mM choline chloride, 3 mM KCl, 2.4 mM CaCl2,1.3 mM $MgCl_2$, 26 mM $NaHCO_3$,1.24mM NaH_2PO_4, and 10 mM glucose. Slices were immediately placed for 1 h at 35°C in incubation chambers filled with carbogen-bubbled aCSF (with choline chloride replaced by a stoichiometric amount of NaCl).

Eight slices were collected per mouse and incubated in aCSF for 1 h at 37°C to recover from sectioning. This was followed by incubation with Zymosan beads (500 μg/mL, 100 μL per slice) at 37°C for an additional hour. After washing slices 3 times with 1X PBS, they were fixed in 4% PFA for 1 h at RT followed by 3 washes with 1X PBS and immunostaining. Fixed slices were incubated for 3 h with blocking solution (5% normal goat serum, 0.3% Triton X- in PBS) and incubated for 5 days with antibodies Iba1 and anti-GFP in the same solution. This was followed by staining with secondary Alexa Fluor 647 conjugated goat-*anti*-rabbit and Alexa Fluor 488 goat anti-chicken antibodies at 4°C for 4 h. After PBS washes, slices were mounted with anti-fade mountant and images were acquired with the confocal Zeiss LSM880 microscope. Brain regions that showed bead uptake were imaged using a 20x/0.8 air objective and with a 1.5 μm spaced z-tack spanning the beads in the field of view.

Images recorded from the *ex vivo* slice assay were analyzed with a batch processing script written for ImageJ. The pan-microglia staining (IBA1) was used to detect all microglia following pre-processing (i.e., local background filtering, median filtering), fixed intensity thresholding, and post-processing (i.e., particle size filtering). Microglia were distinguished as mouse or human microglial cells based on the presence or absence of the GFP reporter signal in human and mouse microglia respectively. Phagocytosed beads were detected following pre-processing (i.e., local background filtering, Gaussian blurring, Laplacian filtering), maximum finding with image segmentation based on a seeded watershed algorithm, and post-processing (i.e., particle size filtering and connected component labeling). For each microglia in the image, the number of phagocytosed beads was expressed for further analysis and images for visual verification of the image analysis process were created. The phagocytic activity was measured based on several parameters in both human and mouse cells on each slice. The treatment was applied on the level of the slice (i.e., the experimental unit), and slices were derived from multiple mice and thus nested within this factor. Because the number of slices derived from each mouse was not fixed, a linear mixed model was modeled per readout in R (*lmerTest::lmer*) with fixed factors (treatment, cell type and their interaction)

and random factors (mouse). The model was reduced to exclude the interaction effect if it was not significant (p-value >0.05). Statistical differences were indicated as follows: 0.05 < p (*), 0.01 < p (**), and $p < 0.001$ (***).

Generation of chimeric mice

iHPC cells were thawed in iHPC base medium and cultured for 3 days in iMGL differentiation medium to obtain iMGL progenitors (refer to supplementary methods for details on iMGL generation). Cells were harvested and resuspended at 250,000 cells/μL in 1X PBS and maintained on a shaker at room temperature for engraftment. Surgery was performed when the pups were between 3 and 4 days old (P3-4). Mice were placed on a neonatal stereotaxic frame adaptor that was cooled to 4°C with dry ice immersed in 70% ethanol. Once cryo-induced anesthesia was performed, 2 μL of iMGL in 1X PBS were injected in both lateral ventricles (anteroposterior +1.50; mediolateral ±1.00 for the left and right hemisphere; dorsoventral +1.70) using a stereotaxic device (Neurostar) adapted with a 10 μL 32G Hamilton syringe. Cells were injected over the course of 90 s, followed by a 30 s pause and a slow needle retraction. The needle was rinsed several times in PBS, 70% ethanol, and PBS before each use. Following surgery pups were allowed to recover on a heated pad and were returned to their litters. Tissue collection was performed at various timepoints post engraftment following general anesthesia with 5% isoflurane in 2.4 L/min O_2 and transcardial perfusion for 5 min with 1X HBSS (10 U/ml heparin) using a peristaltic perfusion system with a flow rate of 2 mL/min. Hemispheres from each brain were collected and stored or processed separately according to the experimental readout (refer to supplementary methods for additional details). All experiments and procedures involving animals were performed in the AAALAC-accredited UCB animal facility, and according to protocols approved by the UCB Ethical Committee for Animal Experimentation. All procedures comply with the European (Directive 2010/63/EU) and local legislation on the protection of animals used for scientific research.

Systemic LPS administration

Four-month-old chimeric mice were injected i.p. with 5 mg/kg LPS. Tissue collection for mass cytometry was performed following general anesthesia and transcardial perfusion as described above. For tissue processing method for mass cytometry and CyTOF analysis refer to supplementary material.

AAV generation and intra-striatal injections

AAV6-mAIF1-RFP, AAV2-CAG-RFP, AAV9-CAG-RFP were generated at Vector Biolabs. AAV preparations were titre-matched to have equal injections volumes (1 μL), at 1×10^9 vg for AAV2, AAV6, AAV9 and an additional higher dose at 1×10^{10} vg for AAV9. The carrier solution contained PBS with 0.001% pluronic F-68 Non-ionic Surfactant. Endotoxin levels were measured at Vector Biolabs and recorded at below 1 EU/ml for all the serotypes.

Four-month-old chimeric mice were anesthetized with isoflurane at 2% in 2.4 L/min O_2. Analgesic Buprenorphine (0.1 mg/kg) was administered subcutaneously prior to stereotactic surgery. Fur was shaved and a scalp incision was performed followed topical application of xylocaine for additional local analgesia. A burr hole was created to enable bilateral striatal injections guided by stereotactic coordinates: anteroposterior +0.20; mediolateral ±2.00 for the left and right hemisphere; dorsoventral −3.20). To reduce AAV inoculation volume to 1 μL and increase precision a 10-μL Hamilton syringe with a 32 G needle was used coupled with an infusion pump flow of 500 nL/min. Following injection, the syringe was maintained in position for up to 60 s to facilitate the distribution of the injectant within the brain and minimize any backflow upon needle withdrawal. The incision was closed using Vicryl 3.0 suture thread. Mice were sacrificed 8 weeks following AAV administration.

QUANTIFICATION AND STATISTICAL ANALYSIS

All statistical analyses in this study were carried out as described in the corresponding method sections, and the exact n numbers for each experiment, as well as the significance indicators (number of stars corresponding to the p-value thresholds), are clearly shown in the figure insets throughout the manuscript. Statistical approaches included ANOVA-based comparisons with post-hoc testing, linear mixed-effects models for slice-based phagocytosis assays, and differential expression analyses for single-cell and spatial transcriptomic datasets, with full details provided in the CyTOF, single-cell sequencing, and spatial transcriptomics method subsections. Significance was generally defined by p-value thresholds annotated in the figures, and the manuscript reports mean values with measures of variability as indicated in the corresponding legends. Randomization was performed at the level of assigning pups to engraftment and treatment groups, and analyses, including imaging, CyTOF gating, and computational workflows, were conducted blinded to group allocation. Sample sizes followed common practice in chimeric microglia and AAV studies and were guided by prior experiments establishing variability in engraftment and immune activation. Data or samples were excluded only in cases of predefined technical failures such as unsuccessful engraftment, compromised AAV injections, or low-quality sequencing libraries that did not meet objective QC thresholds. Assumptions for parametric tests were evaluated using standard diagnostic checks as appropriate, while transcriptomic analyses employed the established pipelines described in their respective sections. Together, these procedures ensured consistent and transparent quantification across imaging, cytometry, and sequencing datasets, with all statistical information traceable via the figure insets and detailed method subsections.